Numerics of the lattice Boltzmann method: Effects of collision models on the lattice Boltzmann simulations

Li-Shi Luo (罗礼诗), Wei Liao (廖伟), Xingwang Chen (陈兴旺), Yan Peng (彭艳), and Wei Zhang (张炜)

Phys. Rev. E **83**, 056710 — Published 26 May 2011

DOI: 10.1103/PhysRevE.83.056710

Numerics of the lattice Boltzmann method: Effects of collision models on the lattice Boltzmann simulations

Li-Shi Luo (罗礼诗),[1,*] Wei Liao (廖伟),[1,†] Xingwang Chen (陈兴旺),[1] Yan Peng (彭艳),[1,‡] and Wei Zhang (张炜)[2,§]

[1] *Department of Mathematics & Statistics and Center for Computational Sciences Old Dominion University, Norfolk, VA 23529, USA*

[2] *Department of Fluid Machinery and Engineering, School of Energy and Power Engineering Xi'an Jiaotong University, Xi'an 710049, Shaanxi Province, P. R. China*

Abstract

We conduct a comparative study to evaluate several lattice Boltzmann (LB) models for solving the near incompressible Navier-Stokes equations, including the lattice Boltzmann equation with the multiple-relaxation-time (MRT), the two-relaxation-time (TRT), the single-relaxation-time (SRT) collision models, and the entropic lattice Boltzmann equation (ELBE). The lid-driven square cavity flow in two dimensions is used as a benchmark test. Our results demonstrate that the ELBE does not improve the numerical stability of the SRT or the lattice Bhatnagar-Gross-Krook (BGK) model. Our results also show that the MRT and TRT LB models are superior over the ELBE and LBGK models in terms of accuracy, stability, and computational efficiency, and that the ELBE scheme is the most inferior among the LB models tested in this study, thus is unfit for carrying out numerical simulations in practice. Our study suggests that, to optimize the accuracy, stability, and efficiency in the MRT model, it requires at least three independently adjustable relaxation rates: one for the shear viscosity ν (or the Reynolds number Re), one for the bulk viscosity ζ, and one to satisfy the criterion imposed by the Dirichlet boundary conditions which are realized by the bounce-back type boundary conditions.

PACS numbers: 47.11.-j, 47.15.-x, 47.45.Ab

Keywords: lattice Boltzmann equation; entropic lattice Boltzmann scheme; accuracy; stability; efficiency; 2D lid-driven square cavity flow

* lluo@odu.edu; http://www.lions.odu.edu/~lluo; Corresponding author. Tel.: +1 (757) 683-5295, FAX: +1 (757) 683-3885.

† wliao@odu.edu

‡ ypeng@odu.edu

§ zhangwei@stu.xjtu.edu.cn

I. INTRODUCTION

The lattice Boltzmann equation (LBE) has been used to solve a wide range of of problems in computational fluid dynamics (CFD) (cf. reviews [1, 2] and references therein). There are several variations of the LBE, including the lattice Bhatnagar-Gross-Krook (LBGK) model or single-relaxation-time (SRT) model, the entropic model [3, 4], and the two-relaxation-time (TRT) [5–7] and multiple-relaxation-time (MRT) [8–11] models. All these LB models can be derived from the linearized Boltzmann equation [12, 13], and the difference between them resides in their collision terms. The lattice BGK (LBGK) model is the simplest in appearance and thus is also the most popular one. However, the LBGK model has several inherent deficiencies including numerical instability and inaccurate boundary locations [14, 15]. The entropic LBE (ELBE) is intended to overcome the numerical instability of the LBGK model [3, 4]. The MRT-LB model is the most general form derived from the linearized collision model within the theoretical framework of the LBE and kinetic theory — it includes all possible degrees of freedom to optimize the LBE, and it has been shown to be superior over the SRT models in terms of accuracy, stability, and computational efficiency [10, 15, 16]. The TRT model allows only two most important relaxation rates in the LBE; it retains some advantages of the MRT model in terms of accuracy and stability, while maintaining the simplicity of implementation and hence the computational efficiency.

While the aforementioned LB models have existed for quite some time, there has never been a comprehensive comparative evaluation to quantitatively assess the efficacy of these LB models for solving problems in CFD. In this work, we intend to compare the LBGK, ELBE, MRT, and TRT models in terms of their accuracy, stability, and computational efficiency for solving the incompressible Navier-Stokes equations in two dimensions (2D). We will use the lid-driven square cavity flow in 2D as a benchmark test.

The remainder of the paper is organized as follows. Sec. II provides a succinct introduction of the LB models including the MRT, TRT, LBGK, and ELBE models; it also includes a brief discussion of the bounce-back (BB) boundary conditions (BCs). Sec. III presents the results of this study. We first briefly describe the benchmark test problem: the lid-driven square cavity flow in 2D. The LB results are compared with data obtained by using a pseudo-spectral method with multigrid and singularity subtraction technique [17, 18]. We investigate the abilities of the LB schemes to compute the gross features of the flow, the flow fields near the

boundary, the convergence behavior, the numerical stability, and computational efficiency. Our results expose the inherent deficiencies of the ELBE and LBGK schemes in terms of accuracy, stability, and efficiency. Finally, Sec. IV concludes the paper.

II. LATTICE BOLTZMANN EQUATION

A. Lattice Boltzmann Models

The lattice Boltzmann equation is a discrete system evolves on a d-dimensional lattice $\boldsymbol{x}_i \in \delta_x \mathbb{Z}^d$ and in discrete time $t_n \in \delta_t \mathbb{N}_0 := \delta_t\{0,\, 1,\, \ldots\}$. The lattice Boltzmann equation is derived from the kinetic theory and resembles the discrete velocity model of the Boltzmann equation in some aspects [19]. The discrete velocity set of the LBE, $\mathbb{V} := \{\boldsymbol{c}_i | i = 0,\, 1,\, \ldots,\, b\}$, usually is symmetric, *i.e.*, $\mathbb{V} = -\mathbb{V}$, and has a zero velocity $\boldsymbol{c}_0 = \boldsymbol{0}$. The total number of discrete velocities in $\mathbb{V}$ is $q = (1 + b)$, including one zero velocity and b non-zero ones. An LB model with q velocities in d-dimensional space is usually denoted as DdQq model. In this work, we will use the D2Q9 model on a square lattice, of which the discrete velocity set $\{\boldsymbol{c}_i | i = 0,\, 1,\, \ldots,\, 8\}$ is

$$\boldsymbol{c}_i = \begin{cases} (0,\, 0) & i = 0, \\ (\pm 1,\, 0)c,\ (0,\, \pm 1)c, & i = 1\text{–}4, \\ (\pm 1,\, \pm 1)c, & i = 5\text{–}8, \end{cases} \tag{1}$$

where $c := \delta_x / \delta_t$.

In general, the lattice Boltzmann equation can be concisely written as the following:

$$\mathbf{f}(\boldsymbol{x}_i + \boldsymbol{c}\delta_t, t_n + \delta_t) - \mathbf{f}(\boldsymbol{x}_i, t_n) = \boldsymbol{\Omega}(\mathbf{f}), \tag{2}$$

where the bold-font symbols represent q-dimensional (column) vectors

$$\begin{aligned} \mathbf{f}(\boldsymbol{x}_i + \boldsymbol{c}\delta_t, t_n + \delta_t) =: &(f_0(\boldsymbol{x}_i, t_n + \delta_t), \\ &\ldots,\, f_b(\boldsymbol{x}_i + \boldsymbol{c}_b\delta_t, t_n + \delta_t))^\dagger, \\ \mathbf{f}(\boldsymbol{x}_i, t_n) =: &(f_0(\boldsymbol{x}_i, t_n),\, f_1(\boldsymbol{x}_i, t_n),\, \ldots,\, f_b(\boldsymbol{x}_i, t_n))^\dagger, \\ \boldsymbol{\Omega}(\mathbf{f}) = &(\Omega_0(\boldsymbol{x}_i, t_n),\, \Omega_1(\boldsymbol{x}_i, t_n),\, \ldots,\, \Omega_b(\boldsymbol{x}_i, t_n))^\dagger, \end{aligned}$$

$\dagger$ denotes the transpose operation, $f_i(\boldsymbol{x}_j,\, t_n)$ is the distribution function corresponding to the discrete velocity $\boldsymbol{c}_i$, and Ω_i is the change in f_i due to collisions.

For the purpose of solving the incompressible Navier-Stokes equations, most collision models in the lattice Boltzmann equation (2) are based on the linearized collision operator. This study will focus on the following LB models: the multiple-relaxation-time (MRT) [8–11], two-relaxation-time (TRT) [5–7], single-relaxation-time (SRT) or the lattice Bhatnagar-Gross-Krook (LBGK) [20], and the entropic LB models [3]. We will first discuss the MRT model, of which the collision model can be written as

$$\boldsymbol{\Omega} = -\mathsf{M}^{-1}\cdot\hat{\mathsf{S}}\cdot[\mathbf{m}-\mathbf{m}^{(\mathrm{eq})}], \tag{3}$$

where $\mathbf{m}$ and $\mathbf{m}^{(\mathrm{eq})}$ represent the velocity moments of the distribution functions $\mathbf{f}$ and their equilibria, respectively,

$$\mathbf{m} = (m_0(\boldsymbol{x}_i,t_n),\, m_1(\boldsymbol{x}_i,t_n),\, \ldots,\, m_b(\boldsymbol{x}_i,t_n))^\dagger,$$
$$\mathbf{m}^{(\mathrm{eq})} = (m_0^{(\mathrm{eq})}(\boldsymbol{x}_i,t_n),\, m_1^{(\mathrm{eq})}(\boldsymbol{x}_i,t_n),\, \ldots,\, m_b^{(\mathrm{eq})}(\boldsymbol{x}_i,t_n))^\dagger,$$

M is a $q\times q$ matrix which linearly transforms the distribution functions $\mathbf{f}\in\mathbb{V}\equiv\mathbb{R}^q$ to the velocity moments $\mathbf{m}\in\mathbb{M}\equiv\mathbb{R}^q$,

$$\mathbf{m} = \mathsf{M}\cdot\mathbf{f}, \qquad \mathbf{f} = \mathsf{M}^{-1}\cdot\mathbf{m}, \tag{4}$$

and $\hat{\mathsf{S}}$ is a non-negative $q\times q$ diagonal relaxation matrix [8–11].

The LB method was created as an alternative CFD solver — it is *not* intended as a solver for the Boltzmann equation. The quantities of interest to macroscopic hydrodynamics, such as the density ρ, the flow momentum $\rho\boldsymbol{u}$, and the total energy ρE, as well as their fluxes are (velocity) moments of the single-particle mass distribution function $f(\boldsymbol{x},\boldsymbol{\xi},t)$ in the phase space $\Gamma := (\boldsymbol{x},\boldsymbol{\xi})$, which satisfies the Boltzmann equation, and it is therefore natural to deal with equations of moments (cf. *e.g.*, [21]). The MRT-LBE is formulated in the spirit and tradition of kinetic method in this regard: the collision process is approximated as linear relaxations in the space of moments, and the relaxation rates are directly related to transport coefficients, while the transport process is independently executed in velocity space. The MRT-LBE is not only theoretically elegant, but practically advantageous, as we shall demonstrate through this study.

Corresponding to the nine discrete velocities of the D2Q9 LB model, $\{\boldsymbol{c}_i|i=0,\,1,\,\ldots,\,8\}$, there are nine velocity moments $\{m_i|i=0,\,1,\,\ldots,\,8\}$. The labeling (or the ordering) of these moments is arbitrary and we will use the convention given by Lallemand and Luo [9], that

is, $m_0 = \delta\rho$, $m_1 = e$, $m_2 = \varepsilon$, $m_3 = j_x$, $m_4 = q_x$, $m_5 = j_y$, $m_6 = q_y$, $m_7 = p_{xx}$, and $m_8 = p_{xy}$. The conserved moments in the system are the density $\rho = \rho_0 + \delta\rho$, where $\rho_0 = 1$ and $\delta\rho$ are the mean density and the density fluctuation, respectively, the flow momentum $\boldsymbol{j} = (j_x,\, j_y) = \rho_0 \boldsymbol{u}$, where $\boldsymbol{u} = (u,\, v)$ is the flow velocity. (Because energy is *not* a conserved quantity in the LB models considered in the present, thus these LB models are *athermal*.) The physical significance of the other six non-conserved moments can be found in literature [8–11]. The equilibria of the conserved moments are themselves, and the equilibria of the non-conserved moments are given bellow:

$$e^{(\mathrm{eq})} = -2\delta\rho + \frac{3}{\rho_0}(j_x^2 + j_y^2), \tag{5a}$$

$$\varepsilon^{(\mathrm{eq})} = \delta\rho - \frac{3}{\rho_0}(j_x^2 + j_y^2), \tag{5b}$$

$$(q_x^{(\mathrm{eq})},\, q_y^{(\mathrm{eq})}) = -(j_x,\, j_y), \tag{5c}$$

$$p_{xx}^{(\mathrm{eq})} = \frac{1}{\rho_0}(j_x^2 - j_y^2), \quad p_{xy}^{(\mathrm{eq})} = \frac{1}{\rho_0} j_x j_y. \tag{5d}$$

By considering only $\delta\rho$ in various parts of the equilibria pertaining to the mass conservation, the effects of the round-off error can be reduced [22, 23], especially when $|\delta\rho| \ll 1$. Since the density fluctuation $\delta\rho$ and the flow velocity $\boldsymbol{u}$ are decoupled, the above model approximates incompressible flows [22]. With ordering of the discrete velocities $\{\boldsymbol{c}_i\}$ and the moments $\{m_i\}$ given above, the transformation matrix M is [8–11]:

$$\mathsf{M} = \begin{pmatrix} 1 & 1 & 1 & 1 & 1 & 1 & 1 & 1 & 1 \\ -4 & -1 & -1 & -1 & -1 & 2 & 2 & 2 & 2 \\ 4 & -2 & -2 & -2 & -2 & 1 & 1 & 1 & 1 \\ 0 & 1 & 0 & -1 & 0 & 1 & -1 & -1 & 1 \\ 0 & -2 & 0 & 2 & 0 & 1 & -1 & -1 & 1 \\ 0 & 0 & 1 & 0 & -1 & 1 & 1 & -1 & 1 \\ 0 & 0 & -2 & 0 & 2 & 1 & 1 & -1 & -1 \\ 0 & 1 & -1 & 1 & -1 & 0 & 0 & 0 & 0 \\ 0 & 0 & 0 & 0 & 0 & 1 & -1 & 1 & -1 \end{pmatrix}. \tag{6}$$

Note that rows 4 and 6 uniquely define the ordering (or labeling) of the discrete velocities $\{\boldsymbol{c}_i\}$. Correspondingly, the diagonal matrix of non-negative relaxation rates $0 < s_i < 2$ is given by

$$\mathsf{S} = \mathrm{diag}(0,\, s_e,\, s_\varepsilon,\, 0,\, s_q,\, 0,\, s_q, s_\nu,\, s_\nu). \tag{7}$$

With the equilibria given by Eqs. (5), the first-order non-equilibrium parts of the non-conserved moments are,

$$p_{xx}^{(1)} = -\frac{2}{3s_\nu}\left(\partial_x j_x - \partial_y j_y\right) , \tag{8a}$$

$$p_{xy}^{(1)} = -\frac{1}{3s_\nu}\left(\partial_y j_x - \partial_x j_y\right) , \tag{8b}$$

$$e^{(1)} = -\frac{2}{s_e}\left(\partial_x j_x + \partial_y j_y\right) , \tag{8c}$$

$$\varepsilon^{(1)} = \frac{2}{s_\varepsilon}\left(\partial_x j_x + \partial_y j_y\right) , \tag{8d}$$

$$q_{x,y}^{(1)} = 0\,. \tag{8e}$$

The speed of sound in a quiescent media for the D2Q9 model is

$$c_s = \frac{1}{\sqrt{3}}\,c, \tag{9}$$

and the shear viscosity ν and the bulk viscosity ζ are

$$\nu = \frac{1}{3}\left(\frac{1}{s_\nu} - \frac{1}{2}\right) c\delta_x, \tag{10a}$$

$$\zeta = \frac{1}{6}\left(\frac{1}{s_e} - \frac{1}{2}\right) c\delta_x, \tag{10b}$$

where s_ν is the relaxation rate for the moments p_{xx} and p_{xy}, which are related to the off-diagonal elements of the stress tensor, and s_e is the relaxation rate for the moment e, which is related to the diagonal elements of the stress tensor. The dissipation for (longitudinal) sound waves or density fluctuations in the system is $(\zeta + \nu/2)$.

If we set the relaxation rates for the even-order non-conserved moments (*i.e.*, e, ε, p_{xx}, and p_{xy}) to $s_+ = 1/\tau$ and those for the odd-order ones (*i.e.*, q_x and q_y) to the following [14, 24, 25]:

$$s_q = 8\frac{(2 - s_\nu)}{(8 - s_\nu)} = 8\frac{(2\tau - 1)}{(8\tau - 1)} = \frac{16\nu}{8\nu + 1}, \tag{11}$$

then the MRT model becomes the two-relaxation-time (TRT) model [5–7]. If we set all relaxation rates $\{s_i\}$ equal to $1/\tau$, then the MRT model reduces to the lattice Bhatnagar-Gross-Krook (LBGK) model with single-relaxation-time (SRT), of which the equilibrium distribution functions are:

$$f_i^{(\mathrm{eq})} = w_i\left[\delta\rho + \rho_0\left\{\frac{\boldsymbol{c}_i\cdot\boldsymbol{u}}{c_s^2} + \frac{1}{2}\left(\frac{(\boldsymbol{c}_i\cdot\boldsymbol{u})^2}{c_s^4} - \frac{\boldsymbol{u}\cdot\boldsymbol{u}}{c_s^2}\right)\right\}\right] , \tag{12}$$

where $w_0 = 4/9$ for $\|\boldsymbol{c}_0\| = 0$, $w_{1,2,3,4} = 1/9$ for $\|\boldsymbol{c}_{1,2,3,4}\| = c$, $w_{5,6,7,8} = 1/36$ for $\|\boldsymbol{c}_{5,6,7,8}\| = \sqrt{2}c$, and $c_s = c/\sqrt{3}$. The collision model in the LBGK equation is

$$\Omega_i = -\frac{1}{\tau}\left[f_i - f_i^{(\mathrm{eq})}\right]. \tag{13}$$

The entropic lattice Boltzmann equation (ELBE) proposed by Ansumali *et al.* [3] has the BGK collision term with the following equilibria:

$$f_i^{(\mathrm{eq})} = w_i \rho \prod_{\alpha=1}^{2} (2 - S_\alpha) \left(\frac{2u_\alpha + cS_\alpha}{c - u_\alpha}\right)^{c_{i\alpha}/c}, \tag{14a}$$

$$S_\alpha := \sqrt{1 + \left(\frac{u_\alpha}{c_s}\right)^2}, \tag{14b}$$

where Greek subscript α denotes the Cartesian coordinates $\{x, y\}$ or $\{1, 2\}$ in 2D, and $c_{i\alpha}/c \in \{-1, 0, +1\}$. The above equilibria can also be re-written as [26]:

$$\begin{aligned} f_i^{(\mathrm{eq})} =& \rho \left(-\frac{1}{2}\right)^{\frac{|c_{ix}|+|c_{iy}|}{c}} \left[\frac{c_s^2}{c^2}(2S_x - 1) + \left(-\frac{u_x c_{ix}}{c^2}\right)^{\frac{|c_{ix}|}{c}}\right] \\ & \times \left[\frac{c_s^2}{c^2}(2S_y - 1) + \left(-\frac{u_y c_{iy}}{c^2}\right)^{\frac{|c_{iy}|}{c}}\right]. \end{aligned} \tag{15}$$

For both the LBGK and ELBE models with one relaxation time τ given above, the shear viscosity ν and the bulk viscosity ζ are given by [9]:

$$\nu = \frac{1}{3}\left(\tau - \frac{1}{2}\right) c\delta_x\,, \quad \zeta = \frac{\nu}{2}\,. \tag{16}$$

The attenuation coefficient (or dissipation) for acoustic waves (or the density fluctuation) in the system is $\zeta + \nu/2 = \nu$ for the LBGK models. Consequently, the LBGK models are prone to numerical instabilities when ν is small (or τ close to 1/2), because there is no ν-independent mechanism to keep the density fluctuation in check.

A few remarks regarding the ELBE model [3] described above are in order here. First of all, the equilibrium moments computed from the equilibrium distributions of Eqs. (14) or (15) with $c_s^2 = c^2/3$ are:

$$e^{(\mathrm{eq})} = 2\rho\,(S_x + S_y - 3)\,, \tag{17a}$$

$$\varepsilon^{(\mathrm{eq})} = \rho\,(2S_x - 3)\,(2S_y - 3)\,, \tag{17b}$$

$$q_{x,y}^{(\mathrm{eq})} = \rho\,(2S_{y,x} - 3)\,\frac{u_{x,y}}{c}\,, \tag{17c}$$

$$p_{xx}^{(\mathrm{eq})} = \frac{2}{3}\,\rho\,(S_x - S_y)\,, \tag{17d}$$

$$p_{xy}^{(\mathrm{eq})} = \rho u_x u_y\,. \tag{17e}$$

Thus, except $p_{xy}^{(\mathrm{eq})}$ and the terms involving $\delta\rho\cdot\boldsymbol{u}$ which are neglected by the incompressibility approximation [22], one difference between the ELBE and MRT-LBE is the $O(u^3)$ terms in the odd-order equilibrium moments, $q_x^{(\mathrm{eq})}$ and $q_y^{(\mathrm{eq})}$, which affect the Galilean invariance of the model [9], while the difference in the even-order equilibrium moments, $e^{(\mathrm{eq})}$, $\varepsilon^{(\mathrm{eq})}$, and $p_{xx}^{(\mathrm{eq})}$, is of the terms of the order $O(u^4)$.

And secondly, based on our experience and understanding of the LBE, it is unclear theoretically how the ELBE with a *constant* relaxation parameter τ can improve the numerical stability of the LBGK scheme, as it has been advocated [3, 4]. Furthermore, if the equilibria of Eqs. (14a) are replaced by their low-order Taylor expansions in $\boldsymbol{u}$, as suggested in [26], then it can be shown *rigorously* that the equilibria of polynomial form cannot admit an H theorem [27, 28] and the ELBE is no longer entropic. In this study we will numerically demonstrate that the ELBE model does not improve the numerical stability of the LBGK model in any way, contrary to previous claims [3, 4].

We would also like to comment on the general characteristics of the LBE. First of all, the relevant physical quantities of the LBE are the conserved quantities, *i.e.*, the density ρ and the momentum $\rho\boldsymbol{u}$ for the athermal LB models — the pressure p and the velocity $\boldsymbol{u}$ are derived or indirect quantities. The conserved quantities, ρ and $\rho\boldsymbol{u}$, obtained with the LBE can only approximate p and $\boldsymbol{u}$, which are the solutions of the incompressible Navier-Stokes equations [29]. Since the density ρ is an intrinsic variable of the LBE, the compressibility associated with the density fluctuation is inherent in the LBE. Thus, the second point is that *all* LB schemes are intrinsically compressible in the sense that the density is an essential variable and the velocity field is never divergence free. The so-called "incompressible" LB schemes (*e.g.*, [22]) can only alter the compressibility effect *quantitatively*, but can never eliminate it entirely. Theoretically, the incompressible Navier-Stokes equations can be derived directly from the Boltzmann equation in the diffusive scaling limit $\delta_x^2/\delta_t = 1$ (cf. [29, 30] and references therein), and the exponential tail of the Maxwellian equilibrium when $\|\boldsymbol{\xi}\| \to \infty$ is indispensable in this derivation. With a set of finite discrete velocities $\{\boldsymbol{c}_i | i = 0, 1, \ldots, b\}$, the LBE cannot possibly satisfy the Poisson equation exactly, which requires the pressure to propagate throughout the system instantaneously, *i.e.*, with a propagating speed of infinity. Thus, the LBE is intrinsically compressible, and can only approximate the incompressible Navier-Stokes equations. The pressure p in the LBE is coupled to the density ρ through a simple equation of state $p = c_s^2\rho$ for ideal gases, and in this way the LBE is related to the

artificial compressibility method [31, 32].

It is also worth noting that the only important distinction between the so-called "incompressible" and the "compressible" LB schemes lies in the acoustics of the system. The speed of the sound waves in the "incompressible" LB schemes is incorrect (cf. Eq. (48) and relevant discussions in [9]),

$$\begin{aligned} C_s &= V\cos\phi \pm \sqrt{c_s^2 + V^2\cos^2\phi} \\ &= V\cos\phi \pm c_s\sqrt{1 + \mathrm{Ma}^2\cos^2\phi}\,, \end{aligned}$$

where $\mathrm{Ma} = V/c_s$, $V = \|\boldsymbol{V}\|$, $\boldsymbol{V}$ is the constant streaming velocity of the media, and ϕ is the angle between $\boldsymbol{V}$ and the wave-vector $\boldsymbol{k}$ of the acoustic waves [9]. In order to have a correct speed of acoustic waves, $C_s = V\cos\phi \pm c_s$, one must use the "compressible" LB schemes, *i.e.*, replacing ρ_0 by ρ in the equilibria of Eqs. (5) and (12). Since we are only concerned with steady-state calculations in this study, while the "incompressible" approximation can improve computational efficiency a little by avoiding the divisions by ρ in computing the equilibria and possibly reduce the compressibility effect [22], its defect in the acoustic propagation will not affect the results negatively.

B. The Bounce-Back Boundary Conditions

The bounce-back boundary conditions in the LBE are used to realize the Dirichlet boundary conditions. The bounce-back boundary conditions are easily to implement: when colliding with an impenetrable wall with a velocity $\boldsymbol{u}_{\mathrm{w}}$, the particle simply reverses its momentum normal to the wall and gains an additional momentum due to the wall velocity $\boldsymbol{u}_{\mathrm{w}}$, *i.e.*,

$$f_{\bar{i}}(\boldsymbol{x}_{\mathrm{b}},\, t+\delta_t) = f_i(\boldsymbol{x}_{\mathrm{b}},\, t) - 2\rho_0 w_i \frac{\boldsymbol{c}_i\cdot\boldsymbol{u}_{\mathrm{w}}}{c_s^2}\,, \tag{18}$$

where $f_{\bar{i}}$ and f_i correspond to the discrete velocity $\boldsymbol{c}_{\bar{i}}$ and $\boldsymbol{c}_i$, respectively, and $f_i(\boldsymbol{x}_{\mathrm{b}},\, t)$ in the right-hand side of Eq. (18) is the post-collision distribution function; $\boldsymbol{c}_{\bar{i}} = -\boldsymbol{c}_i$; the component of $\boldsymbol{c}_i$ normal to the wall is pointing outward from fluid domain to the wall, $\boldsymbol{x}_{\mathrm{b}}$ is a fluid node adjacent to a wall boundary; and $\boldsymbol{u}_{\mathrm{w}}$ is the wall velocity at the point where the particle of the velocity $\boldsymbol{c}_i$ collides with the wall.

The bounce-back boundary conditions are implemented as follows. Beyond the boundary, an extra (ghost) layer of nodes is used to store the distribution functions f_i which move out

of the flow domain in the advection step; the collisions between these particles and the wall are accomplished by reversing themselves to $f_{\bar{i}}$ and gaining the amount of momentum $-2\rho_0 w_i \boldsymbol{c}_i \cdot \boldsymbol{u}_{\rm w}/c_s^2$, they are then copied to the fluids nodes where they came from through the advection.

The bounce-back boundary conditions have been studied in details and are well understood [14, 24, 25]. The analytic solutions for the LBE with the bounce-back boundary conditions can be obtained for simple flows, such as the Poiseuille and Couette flows [24, 25, 33, 34]. For the Poiseuille flow driven by a constant body force $G = \|\boldsymbol{\nabla} p\|$ and with its walls parallel to lattice lines, the actual channel width H observed in the simulations is given by [14, 24, 25]

$$H^2 = H_{1/2}^2 + 4\Delta^2 - 1, \tag{19a}$$

$$\Delta = \frac{4}{3}\left(\frac{1}{s_\nu} - \frac{1}{2}\right)\left(\frac{1}{s_q} - \frac{1}{2}\right), \tag{19b}$$

where $H_{1/2} := N\delta_x$, N is the number of fluid nodes across the channel. That is, only when the relationship between s_q and s_ν of Eq. (11) is satisfied, $\Delta = 1/2$ and $H = H_{1/2}$; the no-slip boundary conditions at the channel walls are indeed satisfied at the $\delta_x/2$ beyond the last fluid nodes; and the maximum velocity at the channel center line is $U_{\max} = GH^2/8\nu$. If $H \neq H_{1/2}$, then the LB solution is *inconsistent* with the incompressible Navier-Stokes solution we desire.

For the ELBE and the LBGK schemes with only one relaxation parameter τ, Eq. (19b) becomes

$$\Delta = \frac{4}{3}\left(\tau - \frac{1}{2}\right)^2 = 12\nu^2\,.$$

Therefore, $\Delta = 1/2$ if and only if $\nu = 1/(2\sqrt{6})$ (or $\tau = 1/2 + \sqrt{6}/4 \approx 1.1123$). In the interval $1/2 < \tau \leq 1/2 + \sqrt{6}/4$, we have $-1 < (4\Delta^2 - 1) \leq 0$ or $0 < \Delta \leq 1/2$. Consequently the error of the inaccurate boundary location is within one lattice spacing δ_x. This explains why the LBGK simulations of flows of high Reynolds number with $\tau < 1$ have relatively small errors at the boundary. Since this error at the boundary is quadratic in ν (or τ), it becomes considerable or even intolerable when $\tau \gg 1$, which is the case for the Stokes or creeping flows and is practiced in simulations of flow through porous media [14, 15]. This error of the LBGK schemes with the bounce-back type boundary conditions is ostentatiously manifested in simulations of flow through porous media with very low Reynolds numbers —

the permeability obtained by the LBGK schemes is viscosity dependent, which is unphysical [14, 15].

Due to the intuitive nature of the bounce-back boundary conditions, it is often mistakenly *assumed* that, in the ELBE and LBGK schemes, the imposed Dirichlet boundary conditions are indeed satisfied either right on the last fluid nodes adjacent to boundary, or one half or one full grid spacing beyond them. This forms the basis of the misguided idea that the non-zero velocity in the vicinity of the last fluid nodes can mimic the Knudsen layer in rarefied flows (*e.g.*, [35–37]). However, a close examination shows that the ELBE or LBGK schemes with the BB type BCs are inadequate to model the Knudsen layer for at the following reasons. The first is that theoretically the LBE is a truncated model valid for the Navier-Stokes equations, and is incapable of modeling higher-order moments of the distribution function [38–41]. And the second is that the velocity near the boundary depends on the grid resolution N thus the solution with fixed Re, Ma, and Kn does not converge as N increases [41]. A more detailed discussion of this point is deferred to Sec. III C.

III. RESULTS AND DISCUSSIONS

A. Lid-driven square cavity flow in 2D

We will use the lid-driven square cavity flow in two dimensions (2D) as a test case to compare the lattice Boltzmann models. The 2D lid-driven flow prescribed by the 2D incompressible Navier-Stokes equation on a square domain $\Omega := (x, y) \in [0, L] \times [0, L] = [0, 1] \times [0, 1]$:

$$\begin{aligned} &\partial_t \boldsymbol{u} + \boldsymbol{u} \cdot \boldsymbol{\nabla} \boldsymbol{u} = -\boldsymbol{\nabla} p + \nu \nabla^2 \boldsymbol{u}, \quad \boldsymbol{\nabla} \cdot \boldsymbol{u} = 0\,, \\ &\boldsymbol{u}(x, 1) = (U, 0),\ \boldsymbol{u}(x, 0) = \boldsymbol{u}(0, y) = \boldsymbol{u}(1, y) = \boldsymbol{0}\,, \end{aligned} \tag{20}$$

where $\boldsymbol{u}(\boldsymbol{x}, t)$ and $p(\boldsymbol{x}, t)$ are the velocity and the pressure field, respectively, and U is the sliding velocity of the top wall. The Reynolds number of the flow is defined by the sliding velocity U, the dimension L of the cavity, and the viscosity ν, *i.e.*, $\mathrm{Re} = UL/\nu$.

The 2D lid-driven square cavity flow has been studied extensively and employed by many as a benchmark test (cf., *e.g.*, [17, 18, 42–45]). While the geometry of the flow domain is simple, the flow exhibits complicated features. Small vortexes developed at the corners and

other locations can be difficult to capture numerically for they are weak and small. The flow becomes unsteady when the Reynolds number is beyond a certain critical value, and eventually becomes turbulent. In this work we will restrict ourselves to the steady states of the flow with Re = 100, 400, and 1,000. The criterion for reaching steady state in the LB simulations is given by

$$\frac{\sum_i \|\boldsymbol{u}(\boldsymbol{x}_i,\, t_n + 1000\delta_t) - \boldsymbol{u}(\boldsymbol{x}_i,\, t_n)\|_2}{\sum_i \|\boldsymbol{u}(\boldsymbol{x}_i,\, t_n)\|_2} < 10^{-12}, \tag{21}$$

where $\|\boldsymbol{u}\|_2$ denotes the L^2 norm of $\boldsymbol{u}$. We will compare the LB simulations with the results obtained by using an explicit Chebyshev pseudo-spectral (PS) multigrid (MG) method (cf. [18] and refs. therein) together with a singularity subtraction technique (cf. [17] and refs. therein) to deal with the corner singularities. With singularity subtraction technique, PS-MG methods can yield very accurate results effectively and efficiently [17, 18].

For the LB simulations, the viscosity in the units of δ_x and δ_t is determined by

$$\nu = \frac{UL}{\mathrm{Re}}\,, \tag{22}$$

where $U = 0.1c$ unless other stated and $L = N_x\delta_x$. Therefore,

$$\tau = \frac{1}{s_\nu} = 3\nu + \frac{1}{2} = \frac{3UN\delta_x}{\mathrm{Re}} + \frac{1}{2}. \tag{23}$$

For the MRT and TRT models, Eq. (11) is used to determine the value of s_q, which is the relaxation rate for the heat fluxes q_x and q_y. The other two relaxation rates, s_e for the energy mode and s_ε for the energy square mode, are set to 1.64 and 1.54, respectively [9]. We use the bounce-back boundary conditions in the LB simulations. The nodes on the top two corners belong to the moving lid in the LB simulations.

The value of $U = 0.1c$ is not chosen entirely arbitrary — it is a compromise between accuracy and computational efficiency. The value of U cannot be too large or the LB code becomes unstable. Also the compressibility error in the LBE is of $O(U^2)$ [29, 43], therefore U should be as small as possible for the sake of accuracy. As a practical rule, one should restrict $\|\boldsymbol{u}(\boldsymbol{x},\, t)\| < 0.2$ throughout the entire flow domain and for all time, so that flow is nominally incompressible. On the other hand, larger U also means better computational efficiency, because the number of iterations to reach steady state, N_t, is proportional to the hydrodynamic diffusive time scale in the system, *i.e.*, $N_t \propto N^2/\nu = \mathrm{Re}N/U = c_s\mathrm{Re}N/\mathrm{Ma}$. Thus the number of iterations N_t and the computational time are inversely proportional

to U with both the mesh resolution N and the Reynolds number Re fixed. One can also see that increasing U effectively increases the Courant-Friedrichs-Lewy (CFL) number, thus decreases the computational time as a consequence [57].

In pseudo-spectral methods, both the stream function ψ and the vorticity ω can be obtained analytically from the velocity $\boldsymbol{u}$. In the LBE, ψ is computed by using Simpson's rule for numerical integration:

$$\begin{aligned}\psi(x_{i+1},\, y_j) =& \psi(x_{i-1},\, y_j) - \frac{\delta_x}{6}\left[v(x_{i-1},\, y_j)\right. \\ &\left. +4v(x_i,\, y_j) + v(x_{i+1},\, y_j)\right] ,\end{aligned} \tag{24}$$

where $\psi(x = 0,\, y) = 0$, and the vorticity ω are computed from $\boldsymbol{u}$ by using the following finite difference formulas:

$$\begin{aligned}\partial_x u(x_i,\, y_j) \approx& u(x_{i+1},\, y_j) - u(x_{i-1},\, y_j) \\ &- \frac{1}{4}\left[u(x_{i+1},\, y_{j+1}) - u(x_{i-1},\, y_{j+1})\right. \\ &\left. -u(x_{i-1},\, y_{j-1}) + u(x_{i+1},\, y_{j-1})\right] ,\end{aligned} \tag{25a}$$

$$\begin{aligned}\partial_y u(x_i,\, y_j) \approx& u(x_i,\, y_{j+1}) - u(x_i,\, y_{j-1}) \\ &- \frac{1}{4}\left[u(x_{i+1},\, y_{j+1}) + u(x_{i-1},\, y_{j+1})\right. \\ &\left. -u(x_{i-1},\, y_{j-1}) - u(x_{i+1},\, y_{j-1})\right] .\end{aligned} \tag{25b}$$

Note that the above formulas used to compute ψ and ω are valid only in the interior of the flow domain $\{(x_i,\, y_j) | 2 \le i \le (N_x - 1),\ 2 \le j \le (N_y - 1)\}$. For the fluid nodes next to the boundary or on the boundary nodes, special consideration must be given because the distance between the last fluid nodes and the boundary is only $\delta_x/2$ as opposed to δ_x (cf. the discussion in Sec. II B). For the fluid nodes next to the left boundary $x = 0$, *i.e.*, $\forall\, (x_1,\, y_j)$ $1 \le j = N$, the following formula is used:

$$\partial_x u(x_1,\, y_j) \approx \frac{1}{3}\left[u(x_2,\, y_j) + 3u(x_1,\, y_j) - 4u(x_0,\, y_j)\right] , \tag{26}$$

where $(x_0,\, y_j)$ denotes a node on the left wall $x = 0$. Note that the velocity $\boldsymbol{u}$ is specified by the boundary conditions at the boundaries, thus the above formula can be simplified to

$$\partial_x u(x_1,\, y_j) \approx \frac{1}{3}\left[u(x_2,\, y_j) + 3u(x_1,\, y_j)\right] ,$$

because $\boldsymbol{u}(x = 0, y) = 0$. Similar formulas can be devised for the right, top, and bottom boundaries. On the boundary, we use Tom's formula to compute the vorticity:

$$\omega(x_0, y_j) = 2v(x_1, y_j)\,, \tag{27a}$$

$$\omega(x_i, y_0) = 2u(x_i, y_1), \tag{27b}$$

$$\omega(x_{N+1}, y_j) = -2v(x_N, y_j)\,. \tag{27c}$$

$$\omega(x_i, y_{N+1}) = 2[U - u(x_i, y_N)]\,. \tag{27d}$$

At the four corners, we simply compute the vorticity as the following:

$$\omega(x_0, y_0) = \omega(x_{N+1}, y_0) = 0\,, \tag{28a}$$

$$\omega(x_0, y_{N+1}) = \omega(x_{N+1}, y_{N+1}) = 2U\,. \tag{28b}$$

B. General flow features

We first compare the pressure $p(x, y)$, the stream function $\psi(x, y)$, and vorticity $\omega(x, y)$ obtained by the pseudo-spectral and LB methods. We found that, in many cases, the results obtained by the MRT-LB and TRT-LB schemes are very close to each other, so are those obtained by the LBGK and ELBE schemes. Therefore we will only show the MRT-LB and ELBE results unless otherwise stated. For the pseudo-spectral method [18], the number of collocation points in each dimension is $N = 96$, and the mesh size for the LB simulations presented in this section is $N_x \times N_y = 129^2$ unless otherwise stated. In LB simulations, we always use an odd number of grid points in each dimension to reduce the oscillations due to the spurious conserved quantities [47, 48].

In Fig. 1, we show p, ψ, and ω with Re $= 100$ ($\tau = 0.887$ and $1/s_q \approx 0.984496125$) obtained by the pseudo-spectral method, the MRT-LB and ELBE schemes. The fields of p, ψ, and ω are normalized by U^2, UL, and U/L, respectively, where U is the sliding velocity of the top boundary and $L = N_x\delta_x = N_x$ is the dimension of the cavity in the lattice units of $\delta_x = \delta_t = 1$. The flow fields obtained by the MRT-LB and ELBE schemes are very close to the PS-MG results in terms of vorticity locations and general features of p, ψ, and ω.

When the Reynolds number Re is increased to Re $= 400$ ($\tau = 0.59675$ and $1/s_q \approx 2.437984495$), as shown in Fig. 2, the pressure field p and the vorticity field ω obtained by using the ELBE scheme start to oscillate in the upper-left corner, while those obtained

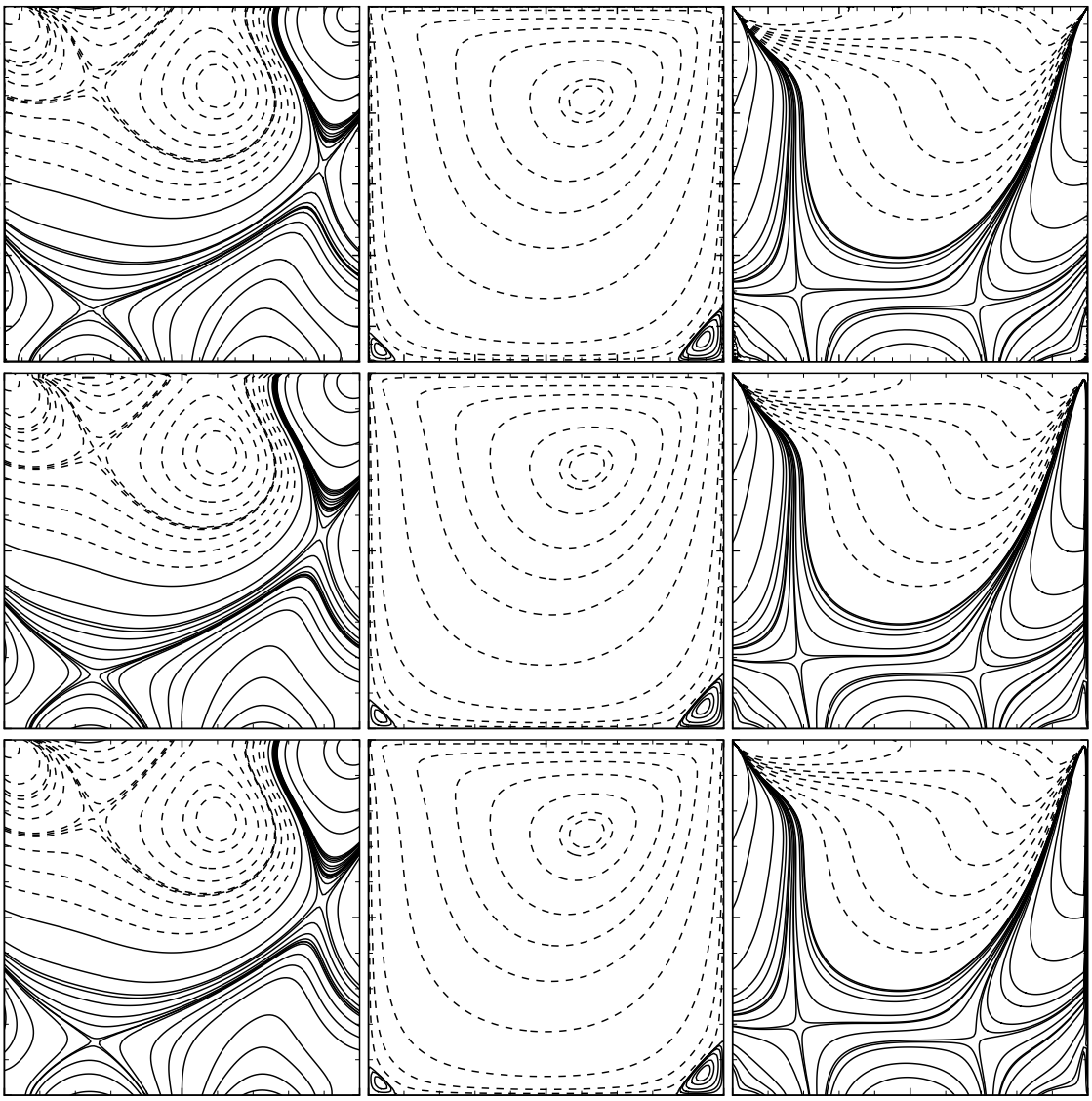

FIG. 1. Re = 100. From left to right: contours of pressure p, stream function ψ, and vorticity ω. From top: the PS-MG method ($N = 96$), and the MRT-LB and ELBE schemes ($N_x \times N_y = 129^2$). Solid and dashed lines denote contours of positive and negative values, respectively.

by the MRT-LB and TRT-LB schemes remain close to the pseudo-spectral results without oscillations. The oscillations in the ELBE simulations are in part due to the fact that there is insufficient dissipation to the higher order moments in the model. This is evident because the results obtained by using the TRT-LB scheme do not exhibit any oscillation, that is, a larger dissipation to the heat flux modes (q_x, q_y) is sufficient to prevent the oscillation.

When the Reynolds number Re is further increased to Re $= 1,000$ ($\tau = 0.5387$ and $1/s_q \approx 5.34496124$), as shown in Fig. 3, the oscillations in both the pressure field p and

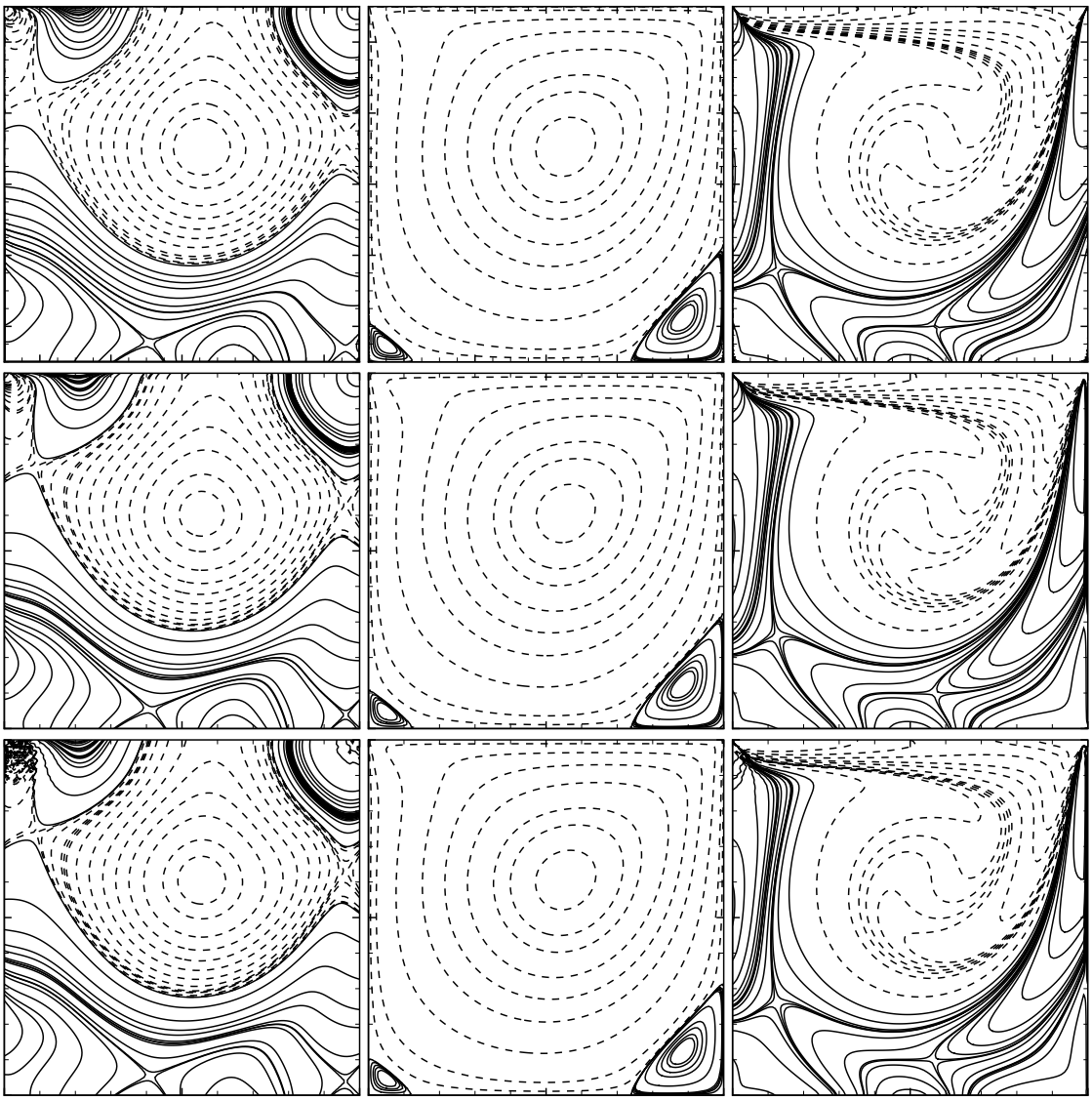

FIG. 2. Re = 400. Similar to Fig. 1.

the vorticity field ω obtained by using the ELBE scheme become quite severe, for lack of sufficient dissipation to the higher order moments, while the results obtained by both the MRT-LB and TRT-LB schemes remain free of oscillations and close to the pseudo-spectral solutions.

We observe that the general features in the vorticity fields obtained by both the TRT-LB and MRT-LB schemes agree with the pseudo-spectral results better than the pressure field p does. This is expected because the pressure field p in the LBE is not solved as accurately as the velocity field $\boldsymbol{u}$ [29]. To make a closer examination of the oscillations in p and ω observed in the ELBE and LBGK schemes, we also carry out simulations at Re = $1,000$

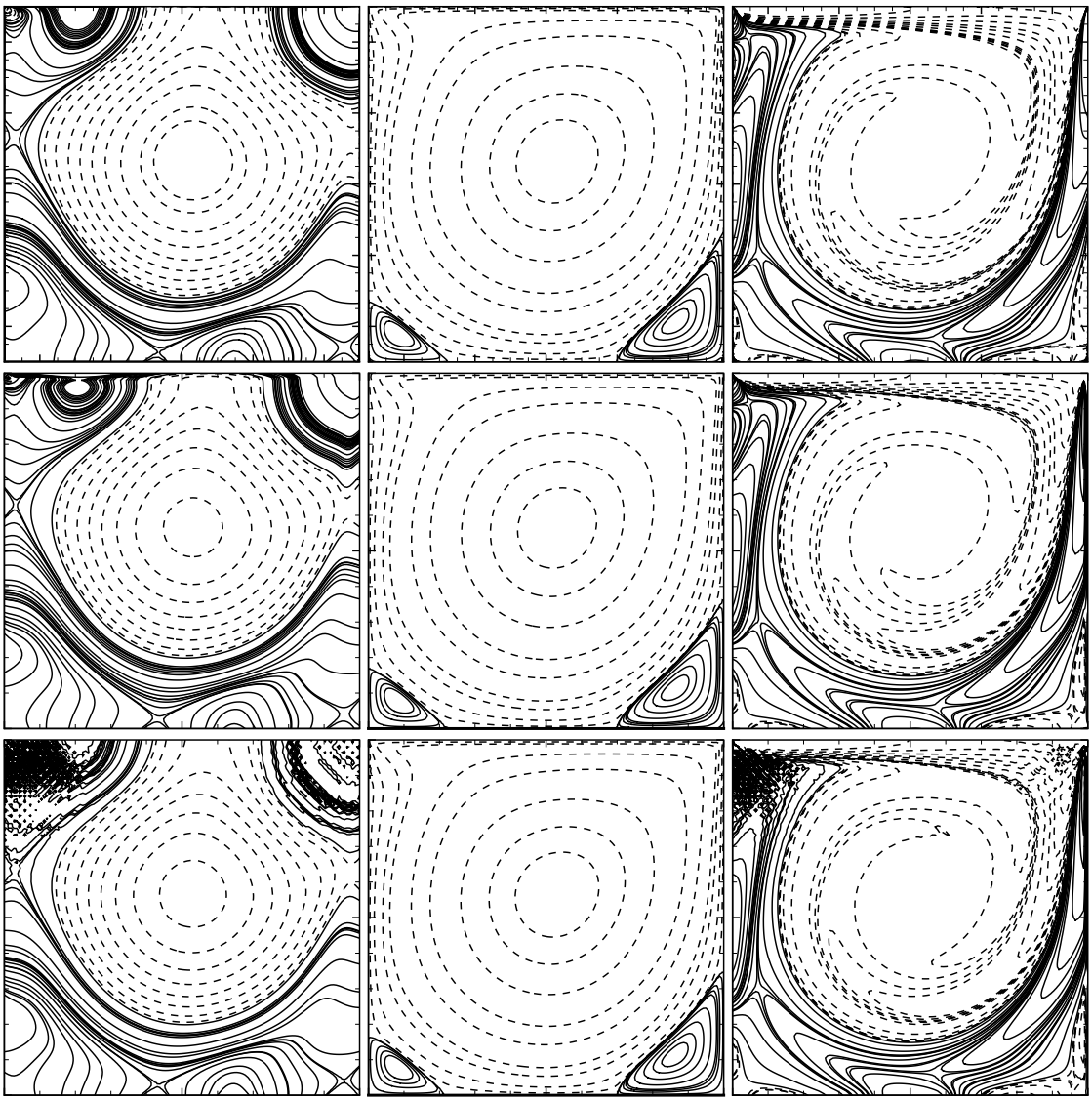

FIG. 3. $\mathrm{Re} = 1,000$. Similar to Fig. 1.

with a larger mesh size of $N^2 = 257^2$ ($\tau = 0.5771$). In Fig. 4 we show the pressure field p and the vorticity field ω in the small area at the upper-left corner $(x,\, y) \in [0,\, 0.1] \times [0.9,\, 1.0]$ where the ELBE and LBGK simulations oscillate severely. Because the results of the ELBE and LBGK schemes are so similar to each other, only the results obtained by using the ELBE scheme are shown in Fig. 4. We found that the ELBE scheme does not reduce the oscillations in the simulation; consequently it does not improve the numerical stability of the LBGK scheme, which will be further discussed later. The results obtained by the TRT-LB and MRT-LB schemes are very close to each other and much closer to the pseudo-spectral results (which are not shown in the figure, but will be discussed later). We note that the

LB schemes are only first-order accurate for the pressure field p [29]. Thus, the pressure field obtained by using the LB schemes is expected to be significantly different from the PS solution. We also note that the vorticity field obtained by using the ELBE and LBGK schemes is less oscillatory than the pressure fields.

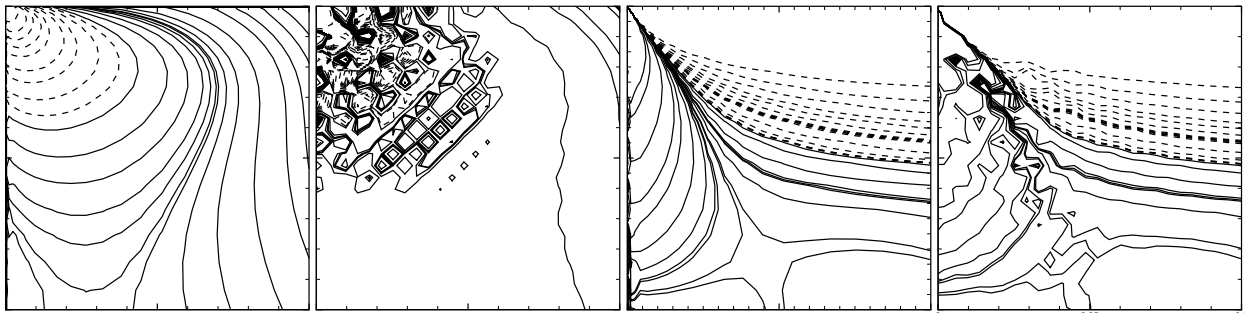

FIG. 4. The pressure field p (two figures on the left) and the vorticity field ω (two figures on the right) at the upper-left corner $(x, y) \in [0, 0.1] \times [0.9, 1.0]$, Re = 1,000. From left to right: p obtained using the pseudo-spectral method ($N = 96$) and the ELBE scheme ($N^2 = 257^2$); and ω obtained using the pseudo-spectral method and the ELBE scheme.

We compile in Table I and Table II, respectively, the positions of the primary and two secondary vortexes, as well as the intensities of the pressure p, the stream function ψ, and the vorticity ω at the vortex centers, which are determined by the locations of local extrema of the stream function ψ. In these tables, we also include the data obtained by using the pseudo-spectral methods [17, 18]. For the data obtained by a pseudo-spectral method [18], the flow fields are interpolated to a very fine, equispaced mesh with the grid spacing of $10^{-6}L$, and the vortex centers and their intensities are found on the fine mesh. In the Tables I and II, blank entries indicate the results obtained by using the LB methods which have at least six significant digits identical to that obtained by using the MRT-LBE with the same mesh size. For example, in Table I, in the case of Re = 100 with $N = 513$, the results obtained by using the TRT-LBE agree with that by the MRT-LBE in at least six significant digits, thus the entries corresponding to the TRT-LB results are left blank in the Table. Note that for the LB results, the vortex centers are determined by finding extrema of the stream function ψ on grid points, thus the error in the vortex centers is of the order $O(1/N)$.

Clearly, the positions of the primary and secondary vortex centers obtained by the LB schemes are identical in most cases, and the difference is only one grid spacing $\delta_x = 1/N$

TABLE I. The center location (x, y), pressure p, stream function ψ, and vorticity ω of the primary vortex.

	N	(x, y)	p	ψ	ω
		Re = 100			
PS	96	(0.615753, 0.737290)	−0.07791293	−0.1035213	−3.168830
MRT	65	(0.623077, 0.746154)	−0.077359	−0.103303	−3.260493
	129	(0.616279, 0.740310)	−0.077366	−0.103483	−3.182492
	257	(0.616732, 0.737354)	−0.077146	−0.103514	−3.175132
	513	(0.615010, 0.737817)	−0.077238	−0.103519	−3.162855
TRT	65		−0.077354	−0.103300	−3.260376
	129		−0.077364	−0.103482	−3.182455
	257		−0.077145		−3.175125
	513				
ELBE	65		−0.077528	−0.103383	−3.273133
	129		−0.077305	−0.103442	−3.189044
	257		−0.077029	−0.103444	−3.180179
	513		−0.077112	−0.103444	−3.167593
LBGK	65	(0.607692, 0.730769)	−0.076922	−0.103434	−3.096890
	129		−0.077379	−0.103490	−3.182824
	257		−0.077106	−0.103494	−3.174138
	513		−0.077187	−0.103493	−3.161545
		Re = 400			
PS	96	(0.5541003, 0.6054134)	−0.07806343	−0.1139895	−2.292390
MRT	65	(0.561538, 0.607692)	−0.076940	−0.113061	−2.286839
	129	(0.554264, 0.608527)	−0.077554	−0.113838	−2.295671
	257	(0.554475, 0.605058)	−0.077635	−0.113958	−2.295325
	513	(0.554581, 0.605263)	−0.077642	−0.113983	−2.294973
TRT	65		−0.077077	−0.113144	−2.288611
	129		−0.077558	−0.113841	−2.295716
	257				−2.295318
	513		−0.077641		−2.294971
ELBE	65		−0.078043	−0.114145	−2.309413
	129		−0.077920	−0.114031	−2.305663
	257		−0.077847	−0.114000	−2.303388
	513		−0.077822	−0.113994	−2.302593
LBGK	65		−0.077889	−0.114159	−2.302237
	129		−0.077742	−0.114022	−2.298109
	257		−0.077669	−0.113991	−2.295796
	513		−0.077644	−0.113985	−2.295001
		Re = 1,000			
PS1	160	(0.5318, 0.5652)	—	−0.1189366	−2.067753
PS	96	(0.5307818, 0.5652325)	−0.08144173	−0.11895958	−2.0686118
MRT	65	(0.530769, 0.561538)	−0.070758	−0.115683	−2.031164
	129	(0.531008, 0.562016)	−0.073607	−0.118406	−2.063210
	257	(0.531128, 0.562257)	−0.074010	−0.118843	−2.067339
	513	(0.531189, 0.566277)	−0.074069	−0.118919	−2.067664
TRT	65		−0.071975	−0.116587	−2.047911
	129		−0.073711	−0.118486	−2.064605
	257		−0.074014	−0.118846	−2.067397
	513				−2.067661
ELBE	129		−0.074672	−0.119253	−2.081538
	257		−0.074461	−0.119117	−2.077452
	513		−0.074422	−0.119098	−2.076384
LBGK	129		−0.074361	−0.119115	−2.073356
	257		−0.074134	−0.118964	−2.069077
	513		−0.074092	−0.118942	−2.067992

at most. The LB results for the vortex positions also agree with those obtained by using

TABLE II. The location (x, y), pressure p, stream function ψ, and vorticity ω of the secondary vortexes.

	N	lower-left secondary vortex					lower-right secondary vortex				
		Re = 100									
		(x, y)		$p \times 10^2$	$\psi \times 10^6$	$\omega \times 10^2$	(x, y)		$p \times 10^2$	$\psi \times 10^5$	$\omega \times 10^2$
PS	96	(0.033586,	0.034560)	1.590806	1.702429	1.198286	(0.943043,	0.062727)	1.935636	1.2738424	3.279431
MRT	65	(0.038462,	0.038462)	1.6287	1.463627	1.7232	(0.946154,	0.069231)	2.0320	1.226275	3.4998
	129	(0.034884,	0.034884)	1.6424	1.787060	1.4701	(0.941860,	0.065891)	2.0545	1.252207	3.8814
	257	(0.036965,	0.033074)	1.6433	1.781289	1.5448	(0.943580,	0.064202)	2.0585	1.269040	3.6066
	513	(0.034113,	0.034113)	1.6470	1.793627	1.4478	(0.942495,	0.061404)	2.0632	1.271244	3.4830
TRT	65				1.462137	1.7231			2.0318	1.225926	3.4999
	129				1.786233	1.4700			2.0544	1.252060	3.8813
	257				1.781069					1.269009	
	513				1.793598					1.271239	
ELBE	65	(0.023077,	0.038462)	1.6508	1.037024	0.4740			2.0366	1.110408	3.4176
	129			1.6405	1.750346	1.4632			2.0451	1.251772	3.8433
	257			1.6372	1.854699	1.5466			2.0458	1.292095	3.5831
	513	(0.034113,	0.036062)	1.6411	1.894922	1.5839	(0.942495,	0.063353)	2.0477	1.300282	3.6342
LBGK	65	(0.023077,	0.038462)	1.6540	1.040556	0.4753			2.0469	1.103691	3.4493
	129			1.6435	1.756372	1.4675			2.0553	1.245085	3.8778
	257			1.6402	1.861059	1.5512			2.0560	1.287105	3.6159
	513	(0.034113,	0.036062)	1.6441	1.901394	1.5886	(0.942495,	0.063353)	2.0579	1.295183	3.6673
		Re = 400									
		(x, y)		$p \times 10^2$	$\psi \times 10^5$	$\omega \times 10^2$	(x, y)		$p \times 10^2$	$\psi \times 10^4$	$\omega \times 10$
PS	96	(0.0507581,	0.0473733)	3.561592	1.411438	6.095086	(0.8854916,	0.1223319)	2.868448	6.445330	4.498006
MRT	65	(0.053846,	0.038462)	3.5478	1.276588	3.7173	(0.884615,	0.130769)	2.8676	6.380941	4.80869
	129	(0.050388,	0.050388)	3.6107	1.409211	6.1506	(0.887597,	0.127907)	2.9286	6.434737	4.63641
	257	(0.048638,	0.048638)	3.6214	1.425964	5.6380	(0.885214,	0.122568)	2.9541	6.441301	4.52944
	513	(0.051657,	0.047758)	3.6218	1.431790	6.0228	(0.885965,	0.121832)	2.9572	6.444459	4.45115
TRT	65			3.5547	1.280803	3.7140			2.8679	6.415618	4.79649
	129			3.6109	1.409436	6.1507			2.9287	6.435241	4.63639
	257			3.6213	1.425921	5.6380			2.9540	6.441246	4.52941
	513				1.431775	6.0227				6.444444	4.45114
ELBE	65			3.6304	0.8986897	3.6154			2.9284	6.121705	4.78454
	129			3.6250	1.315058	6.0880			2.9233	6.409993	4.56471
	257			3.6230	1.394593	5.5897			2.9360	6.459935	4.45056
	513			3.6206	1.412064	5.9729	(0.884016,	0.121832)	2.9392	6.473385	4.49090
LBGK	65			3.6338	0.9117275	3.6448			2.9507	6.079209	4.87065
	129			3.6266	1.333206	6.1393			2.9442	6.377187	4.64669
	257			3.6244	1.412786	5.6359			2.9570	6.430523	4.53112
	513			3.6220	1.430911	6.0226			2.9574	6.443752	4.45123
		Re = 1,000									
		(x, y)		$p \times 10^2$	$\psi \times 10^4$	$\omega \times 10$	(x, y)		$p \times 10^2$	$\psi \times 10^3$	ω
PS1	160	(0.0833,	0.0781)	—	2.334528	3.255861	(0.8640,	0.1118)	—	1.729717	1.109789
PS	96	(0.083276,	0.078090)	3.84669	2.334089	3.544582	(0.864045,	0.111815)	2.815128	1.730292	1.110800
MRT	65	(0.084615,	0.069231)	4.2328	2.039721	2.64440	(0.869231,	0.115385)	3.3005	1.702777	0.993187
	129	(0.081395,	0.081395)	4.4558	2.278163	3.58490	(0.864341,	0.112403)	3.5013	1.730337	1.086797
	257	(0.083658,	0.079767)	4.4860	2.320909	3.65599	(0.861868,	0.110895)	3.5468	1.729997	1.124101
	513	(0.082846,	0.078947)	4.4915	2.331772	3.55657	(0.864522,	0.112086)	3.5500	1.729537	1.103888
TRT	65			4.3129	2.069050	2.66191	(0.853846,	0.100000)	3.3656	1.688924	0.984722
	129			4.4626	2.282009	3.58787			3.5043	1.731326	1.085883
	257			4.4862	2.321087	3.65614			3.5469	1.730064	1.124103
	513			4.4914	2.331765	3.55656				1.729533	1.103887
ELBE	129			4.5203	2.212502	3.58111			3.5382	1.705555	1.074814
	257			4.5064	2.268905	3.63586			3.5396	1.718036	1.104222
	513			4.5044	2.284222	3.53476			3.5367	1.720601	1.111817
LBGK	129			4.5106	2.260153	3.60505			3.5573	1.713561	1.096735
	257			4.4954	2.316249	3.65919			3.5577	1.725431	1.126455
	513			4.4932	2.330706	3.55706			3.5522	1.728455	1.104395

PS-MG methods [17, 18]. The intensities of p, ψ, and ω at the vortex centers obtained by using different methods agree well with each other for the given mesh resolution. For the primary vortex, the intensities of both the stream function ψ and the vorticity ω at the vortex center have agreement of three significant digits, while the pressure p obtained by using the LB schemes only achieves one or two digits agreement with the PS-MG data, and the discrepancy in p clearly grows as Re increases. The errors in the LB results are consistent with the density fluctuation in the system, which is a measure of the compressibility effect in the system. The values of ω, ψ, and p at the primary vortex center are of the order $O(1)$, $O(10^{-1})$, and $O(10^{-2})$, respectively. With $U = 0.1c$ and $\mathrm{Ma} = 0.1/\sqrt{3} \approx 0.1732$, the compressibility effect is of the order $O(\mathrm{Ma}^2) = O(10^{-3})$, which is not negligible when compared with the intensity of p at the vortex centers. A more quantitative discussion of the compressibility effect will be deferred to Sec. III D.

The sizes of the secondary vortexes are much smaller than that of the primary one, and the intensities of p, ψ, and ω at the secondary vortex centers are significantly weaker than those at the primary vortex center, especially at low Reynolds numbers. For example, with $\mathrm{Re} = 100$, at the center of the secondary vortex at the lower-right corner, the intensities of p, ψ, and ω are weaker than their counterparts at the primary vortex center by a factor about 4, 10^4, and 10^2, respectively, and the vortex at the lower-left corner is even smaller and weaker. Nevertheless, the LB simulations are able to quantitatively capture the general flow features.

With $\mathrm{Re} = 1,000$, a tertiary vortex appears at the lower-right corner, which can be accurately captured by the PS method with at least five significant digits (cf. Table 14 in [17]). Both the MRT-LB and TRT-LB schemes can capture the tertiary vortex with a resolution of $N = 129$, but not the ELBE and LBGK schemes. However, with a higher resolution of $N = 257$, all the LB schemes can capture the tertiary vortex, as shown in Fig. 5. We note that the stream function ψ obtained by using the PS-MG method [18] exhibits high-frequency oscillations near the right wall, which affects the results of the tertiary vortex. We tabulate the results for the tertiary vortex in Table III. The values of p, ψ, and ω of the PS-MG method [18] given in Table III are estimated by using data probing tool of Tecplot™, which is used to generate the contour plots of Fig. 5. We note that the stream function ψ at the tertiary vortex center is extremely weak — it is of the order $O(10^{-8})$. With the resolution of $N^2 = 257^2$, the intensities of ψ at the tertiary vortex center obtained

by both the MRT-LB and TRT-LB schemes are about 20% weaker than the very accurate value obtained by using a PS-MG method [17], while the result of the ELBE scheme is weaker than the PS-MG result by a factor about 5. It is remarkable that the LB schemes can capture the tertiary vortex at all, in spite of its minuscule extent and weak intensities.

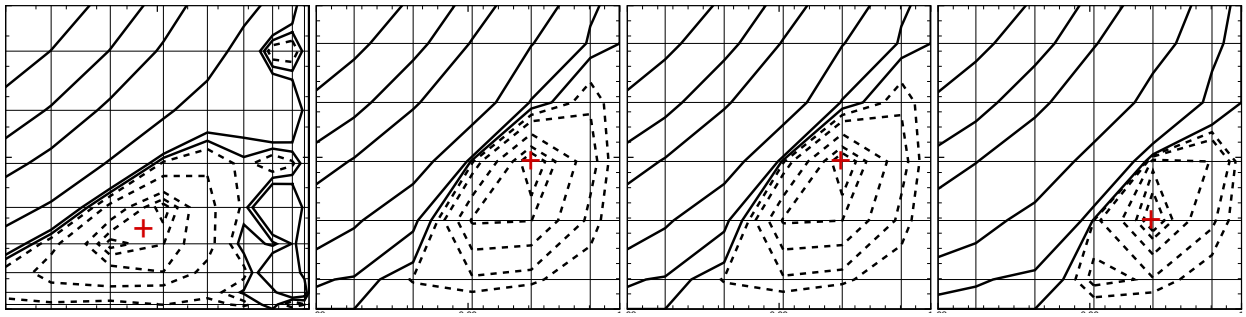

FIG. 5. (Color online) The stream function ψ at the lower-right corner $(x,\, y) \in [0.98,\, 1] \times [0,\, 0.02]$, Re = 1,000. From left to right: PS-MG method ($N = 96$) [18], MRT-LBE, TRT-LBE, and ELBE ($N = 257$). The tertiary vortex is clearly seen. The straight horizontal and vertical lines are the grid lines. The symbol "+" marks the approximated position of the tertiary vortex center.

TABLE III. The center location $(x,\, y)$, pressure p, stream function ψ, and vorticity ω of the tertiary vortex at the lower-right corner.

	N	$(x,\, y)$	$p \times 10^2$	$\psi \times 10^8$	$\omega \times 10^3$
PS1	160	(0.99232, 0.00765)	—	−5.03944	—
PS	96	(0.98913, 0.00534)	2.84	−6.00	8.91
MRT	129	(0.99612, 0.00387)	3.51	−0.976	0.674
	257	(0.99416, 0.00972)	3.55	−4.03	4.84
TRT	129	(0.99612, 0.00387)	3.52	−0.781	0.606
	257	(0.99416, 0.00972)	3.56	−4.07	4.91
ELBE	257	(0.99416, 0.00583)	3.55	−0.937	0.535

C. Flow fields near the boundary

In the previous section, we show that all LB schemes can capture general flow features of the flow, such as locations and intensities of primary and secondary vortexes. We observe that the pressure field near the top sliding lid obtained with the TRT-LB and MRT-LB schemes differ from each other, indicating the effects of the relaxation rates s_e and s_ε on the pressure field p. This is conceivable because s_e directly affects the dissipation of the

acoustics (pressure waves) in the system, while s_ε affects it indirectly through a higher order moment ε.

There are only two adjustable relaxation rates in the MRT-LB scheme: s_e and s_ε; and the other two relaxation rates, s_ν and s_q, are fixed by the Reynolds number Re (cf. Eq. (23)) and the boundary conditions (cf. Eq. (11)), respectively. We fix $s_\varepsilon = 1.9$ and vary s_e in the following test. In addition to the case of $s_e = 1.64$, which is the value used throughout this study unless otherwise stated, we also set $s_e = 1.54$ and 1.9. In Fig. 6 we show the contour plot of the pressure field p and the vorticity field ω at the upper-left corner $(x,\, y) \in [0,\, 0.3] \times [0.7,\, 1.0]$ obtained by using the MRT-LBE with the resolution of $N^2 = 129^2$ and two different values of the relaxation rate $s_e = 1.54$ and 1.64, and compared them with the TRT-LB and PS-MG results [18]. Bear in mind that in the TRT-LB scheme, $s_e = s_\varepsilon = s_\nu$. Because the MRT-LB results for $s_e = 1.54$ and 1.9 are very close to each other, so only the case of $s_e = 1.54$ is shown in Fig. 6. Clearly, the relaxation rate s_e has no observable effect on the vorticity ω, but it affects the pressure p significantly. With $s_e = 1.64$, the contours of the pressure p near the top wall all exhibit a kink, which disappears with $s_e = 1.54$ and 1.9 (which is not shown in the figure), and with the TRT setting ($s_e = s_\varepsilon = s_\nu$). This indicates that the pressure p is affected by not only the relaxation rate s_e, but also s_ε and s_q in a complicated manner.

To further investigate the pressure field near the wall, we show in Fig. 7 the pressure field near the top and the left walls at the fluid nodes adjacent to the boundary, for the case of $\mathrm{Re} = 1,000$. The fluid nodes adjacent to the top driving lid and the left wall are located at $y = \delta_x(1 - 1/2N)$ and $x = \delta_x/2N$, respectively — we assume that the no-slip boundary conditions are satisfied at the line $\delta_x/2$ beyond the last fluid nodes, as discussed in Sec. II B. It can be seen clearly that, when $N = 65$, the pressure field p obtained by using the MRT-LBE with $s_e = 1.64$ has a kink near the top-left corner, where the velocity field is singular mathematically, while the pressure obtained with the TRT-LBE does not exhibit the kink. The kink may indicate that, with the particular choice of $s_e = 1.64$ and $s_\varepsilon = 1.9$, the pressure field obtained by using the MRT-LBE oscillates near the top wall with very short wavelength of about two grid spacing; and the oscillations quickly attenuate. We observe that, with the choice of $s_e = 1.54$ (or 1.9) and $s_\varepsilon = 1.9$, the kink in the pressure field near the top wall disappears completely. Note that, for $\mathrm{Re} = 1,000$, both the ELBE and LBGK schemes diverge with the resolution $N = 65$. For $N = 129$ and 257, the pressure

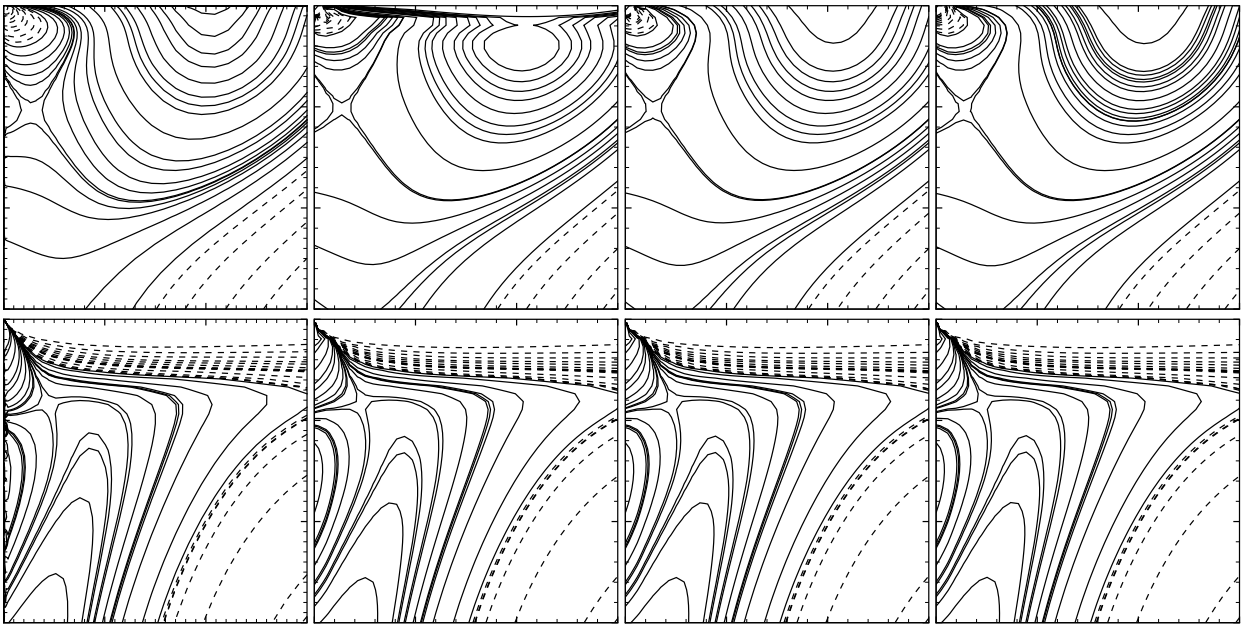

FIG. 6. The pressure field p (top) and the vorticity field ω (bottom) at the upper-left corner $(x,\, y) \in [0,\, 0.3] \times [0.7,\, 1.0]$, Re = 1,000. From left to right: the PS-MG method ($N = 96$) [18], the MRT-LBE with $s_e = 1.64$ and 1.54, and the TRT-LBE ($N = 129$).

field obtained with the ELBE exhibits strong oscillations near the top-left corner, and the magnitude of the oscillations is reduced as N increases while the Reynolds number is fixed. This is understandable because with Re fixed, the value of τ increases linearly as N increases, and so do the viscosity ν and the dissipation to the density fluctuations in the system, as indicated by Eq. (23).

We also study the velocity field $\boldsymbol{u}$ and its gradient $\boldsymbol{\nabla u}$ near the walls. In Fig. 8 we show the gradient of the tangential velocity u along the transverse direction, $\partial_y u(x,\, y)$, and the transverse velocity $v(x,\, y)$ for $\mathrm{Re} = 1,000$ at the fluid nodes adjacent to the driving lid, *i.e.*, $y = (1 - 1/2N)$, for $N = 65$, 129, and 257. Instead of showing $u(x,\, y)$ near the top wall, we choose to show $\partial_y u(x,\, y)$ for it illustrates more clearly the differences between the results obtained by using different methods. The tangential velocity near the top wall, u, has a very sharp gradient in y direction near the top corners, which are captured by the MRT-LB and TRT-LB schemes; and as the resolution N increases, the velocity fields obtained by the MRT-LB and TRT-LB schemes agree with the PS-MG result better and better. The velocity field obtained by using the ELBE oscillates severely near the wall. Similar to the pressure field, oscillations are weakened as N increases.

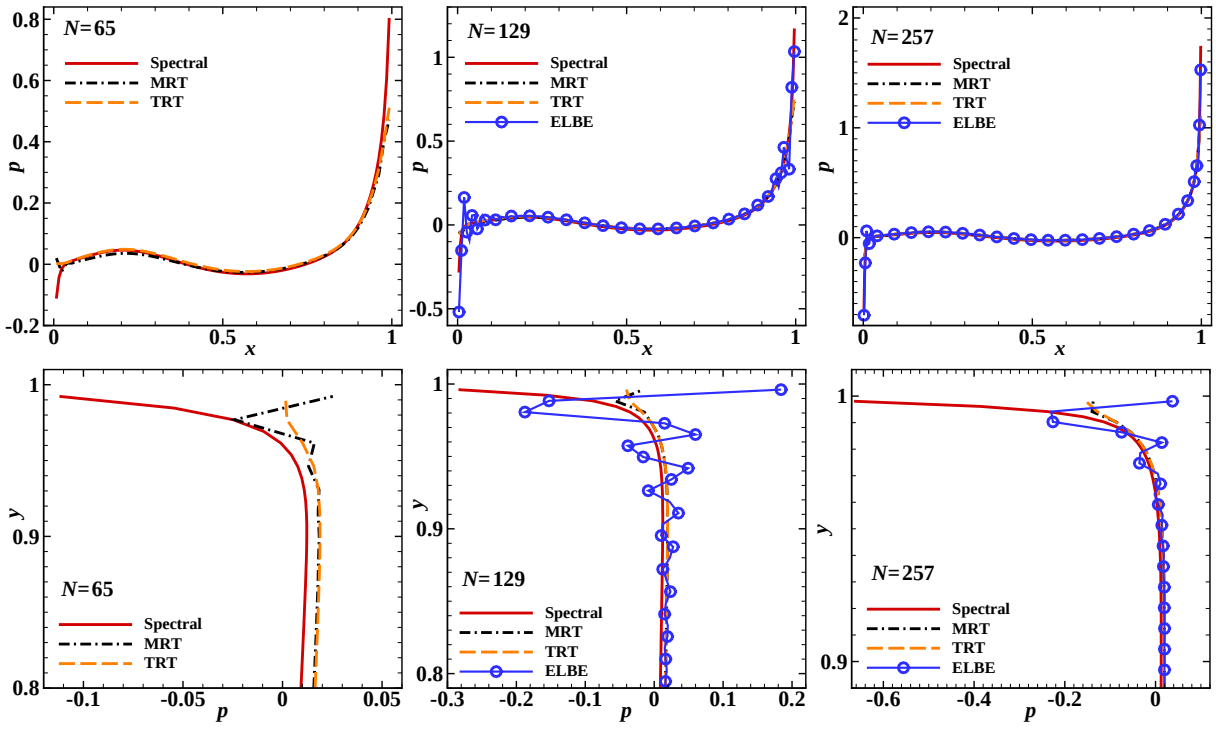

FIG. 7. (Color online) The pressure field near the top (top row) and the left (bottom row) walls, $\mathrm{Re} = 1,000$.

In Fig. 9 we show $\partial v(x,\, y)/\partial x$ and $u(x,\, y)$ near the left wall at $x = \delta_x/2N$ for $N = 65$, 129, and 257. Similar to the results shown in Fig. 8, the velocity field $\boldsymbol{u}$ obtained by using the ELBE scheme exhibits oscillations near the top-left corner, while the velocity field obtained by using the MRT-LB and TRT-LB schemes does not show any oscillation.

It should be emphasized that, for the ELBE and LBGK schemes with one relaxation time and the bounce-back type of boundary conditions, it is impossible to achieve converging results as the mesh is refined because of inaccurate boundary conditions. The inaccurate boundary conditions can lead to severe adverse effects (cf., *e.g.*, [49]). To substantiate this point, we compute the positions where the no-slip boundary conditions are satisfied in the simulations in the middle one-third sections of the left (L), bottom (B), and right (R) walls, *i.e.*, we compute the distance δ between the last fluid nodes to the locations where $\boldsymbol{u} = \boldsymbol{0}$, which is derived from Eq. (19b):

$$\delta = \frac{1}{2} + \sqrt{H_{1/2}^2 + 4\Delta^2 - 1} - H_{1/2}\,. \tag{29}$$

For the Poiseuille flow, $\Delta = 1/2$, thus $\delta = \delta_x/2$ exactly. We use a parabola to fit the velocity tangential to a wall with three points adjacent to the boundary and on the grid

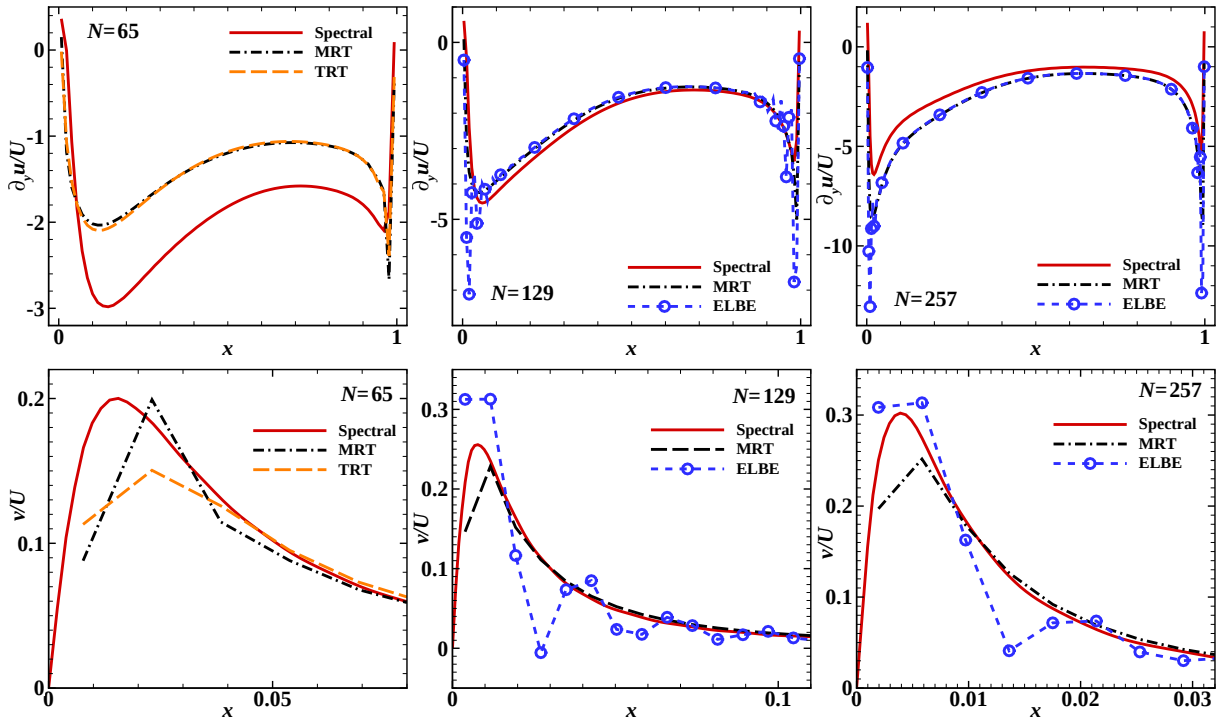

FIG. 8. (Color online) The velocity field $\boldsymbol{u} = (u, v)$ at the last fluid nodes located at $y = 1 - 1/2N$ and adjacent to the top wall, $\mathrm{Re} = 1,000$. $\partial u(x, y)/\partial y$ (top row) and $v(x, y)/U$ (bottom row) at (from left to right): $y = 129/130$, $y = 257/258$, and $y = 513/514$.

line normal to the wall. The least-square fitted parabola is then extrapolated to find the position where the tangential velocity is equal to zero. We observe that in the middle one-third section of the walls, the tangential velocity is at least two orders of magnitude larger than the transverse velocity. In the ideal situation, *i.e.*, the Poiseuille flow, $\delta = \delta_x/2$. We fix the mesh size $N^2 = 65^2$ and 129^2 and vary the value of the viscosity ν (or the relaxation parameter τ). The results are summarized in Table IV.

In Table IV we present the mean value $\bar{\delta}$, the maximum value δ_{M}, and the minimum value δ_{m}, of δ along the left (L), bottom (B), and right (R) walls. Clearly, the value of δ computed by using the MRT-LB and TRT-LB schemes varies very little — at the worst scenario the value of δ deviates from $\delta_x/2$ less than 6%. In contrast, the value of δ obtained by using the ELBE and LBGK schemes can be greater than $3.7\delta_x$, which is more than three grid spacings away from the assumed boundary location.

To further illustrate the inaccuracy of the ELBE and LBGK schemes with the bounce-back boundary conditions, we use the following formula [34] to fit the tangential velocity

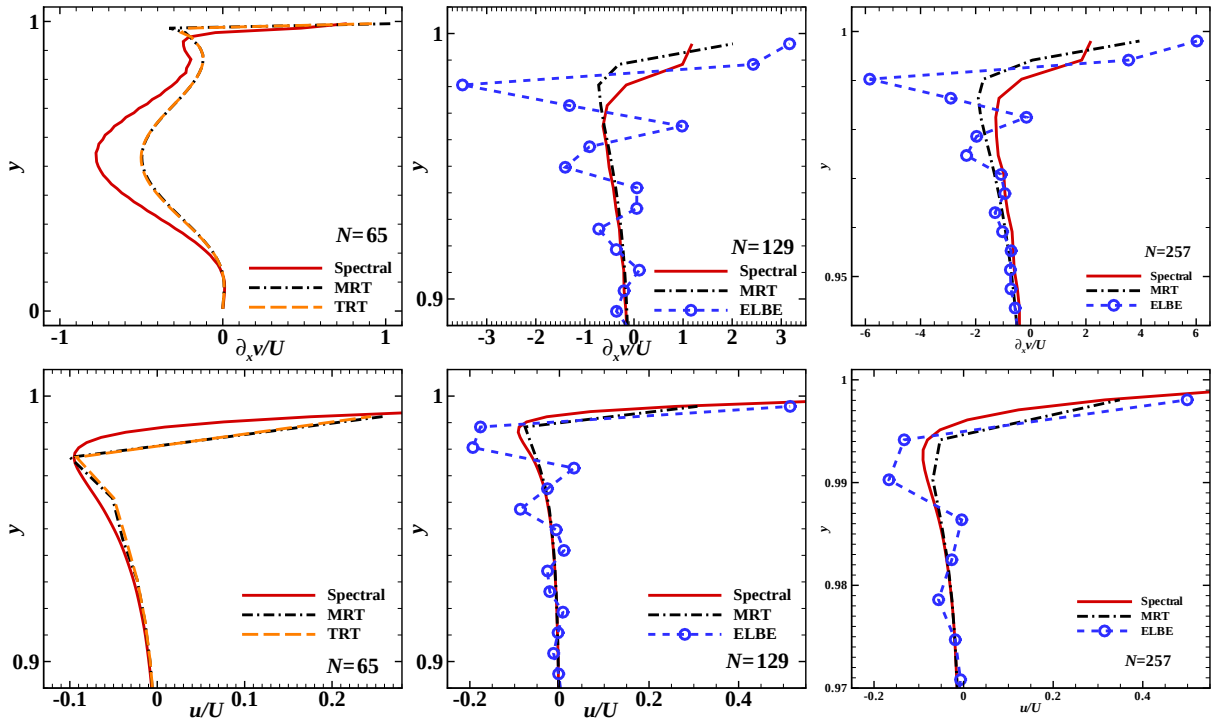

FIG. 9. (Color online) The velocity field at the last fluid nodes located at $x = 1/2N$ and adjacent to the left wall, $\mathrm{Re} = 1,000$. Top row: $\partial v(x, y)/\partial x$ (top row) and $u(x, y)$ (bottom row) at (from left to right): $x = 1/130$, $x = 1/258$, and $x = 1/514$.

along center lines of the cavity,

$$u_i = \frac{4U_*}{N_*^2} i(N_* - i) + U_\mathrm{s}\,, \tag{30a}$$

$$U_\mathrm{s} = \frac{2U_*}{3N_*^2}\left[(2\tau - 1)(4\tau - 3) - 3N_*\right]\,, \tag{30b}$$

where U_* and N_* are the effective maximum velocity and channel width, respectively, which are to be determined by the least-square fitting. For the MRT-LB and TRT-LB schemes, the corresponding formula is:

$$u_i = \frac{4U_*}{N_*^2}(i - 1/2)(N_* + 1/2 - i)\,. \tag{31}$$

We use a small mesh of size $N^2 = 33^2$ and $\tau = 3.0$, which means very small Reynolds number. The tangential velocities along the horizontal center line ($y = 1/2$) near the left wall ($x = 0$) and along the vertical center line ($x = 1/2$) near the bottom wall ($y = 0$) are fitted with Eqs. (30a) and (31). The results are shown in Fig. 10.

The results shown in Fig. 10 indicate that, when the flow is laminar, the tangential velocity near wall is accurately represented by a parabola when the transverse velocity is

TABLE IV. The distance (δ) of the last fluid node to the boundary wall, where $\boldsymbol{u} = \boldsymbol{0}$. L, B, and R indicate the left, bottom, and right wall, respectively. $\bar{\delta}$, $\delta_{\rm M}$, and $\delta_{\rm m}$ denote the averaged, maximum, and minimum values of δ in the middle one-third of a wall, respectively.

		$\tau = 0.55$			$\tau = 1.0$			$\tau = 3.0$			$\tau = 5.0$		
		$\bar{\delta}$	$\delta_{\rm M}$	$\delta_{\rm m}$	$\bar{\delta}$	$\delta_{\rm M}$	$\delta_{\rm m}$	$\bar{\delta}$	$\delta_{\rm M}$	$\delta_{\rm m}$	$\bar{\delta}$	$\delta_{\rm M}$	$\delta_{\rm m}$
		$N^2 = 65^2$											
	L	0.5039	0.5076	0.4979	0.4993	0.4996	0.4985	0.4986	0.4989	0.4980	0.4985	0.4989	0.4977
MRT	B	0.5047	0.5084	0.4985	0.5023	0.5026	0.5017	0.5021	0.5024	0.5016	0.5021	0.5024	0.5016
	R	0.4774	0.4789	0.4719	0.4970	0.4974	0.4964	0.4982	0.4984	0.4979	0.4984	0.4987	0.4980
	L	0.5035	0.5063	0.4985	0.4992	0.4996	0.4983	0.4983	0.4986	0.4975	0.4982	0.4985	0.4973
TRT	B	0.5043	0.5075	0.4988	0.5025	0.5028	0.5019	0.5024	0.5027	0.5020	0.5024	0.5027	0.5019
	R	0.4810	0.4824	0.4742	0.4966	0.4970	0.4960	0.4979	0.4981	0.4976	0.4980	0.4982	0.4976
	L	0.4838	0.5035	0.4783	0.5024	0.5030	0.5007	0.8748	1.1081	0.7056	2.6185	3.7490	1.9473
ELBE	B	0.4983	0.5152	0.4934	0.5052	0.5057	0.5040	0.7535	0.7683	0.7243	1.3025	1.3169	1.2678
	R	0.5070	0.5585	0.4745	0.4985	0.5004	0.4966	0.8928	1.1051	0.7356	2.7151	3.6252	2.1112
	L	0.4838	0.5034	0.4783	0.5024	0.5030	0.5007	0.8748	1.1086	0.7053	2.6174	3.7351	1.9495
LBGK	B	0.4979	0.5138	0.4932	0.5051	0.5058	0.5042	0.7537	0.7685	0.7246	1.3027	1.3171	1.2682
	R	0.5069	0.5580	0.4745	0.4984	0.5004	0.4965	0.8923	1.1045	0.7353	2.7225	3.6500	2.1121
		$N^2 = 129^2$											
	L	0.5010	0.5039	0.4975	0.5000	0.5001	0.4996	0.4996	0.4998	0.4993	0.4996	0.4997	0.4993
MRT	B	0.5015	0.5043	0.4973	0.5006	0.5010	0.5001	0.5006	0.5008	0.5002	0.5006	0.5009	0.5003
	R	0.4896	0.4919	0.4617	0.4988	0.4990	0.4983	0.4994	0.4995	0.4991	0.4995	0.4996	0.4992
	L	0.5009	0.5033	0.4980	0.5000	0.5002	0.4996	0.4996	0.4997	0.4993	0.4995	0.4997	0.4993
TRT	B	0.5014	0.5036	0.4977	0.5007	0.5010	0.5003	0.5007	0.5010	0.5003	0.5006	0.5009	0.5004
	R	0.4909	0.4933	0.4642	0.4987	0.4990	0.4981	0.4993	0.4994	0.4991	0.4994	0.4995	0.4992
	L	0.4886	0.4984	0.4848	0.5018	0.5021	0.5011	0.6369	0.6981	0.5754	1.0796	1.4689	0.8005
ELBE	B	0.4982	0.5113	0.4922	0.5020	0.5025	0.5014	0.6366	0.6466	0.6140	0.9287	0.9546	0.8688
	R	0.5387	0.8978	0.4899	0.4986	0.5003	0.4968	0.6115	0.6911	0.5439	1.0715	1.4629	0.7890
	L	0.4886	0.4985	0.4848	0.5019	0.5021	0.5012	0.6367	0.6978	0.5754	1.0794	1.4690	0.8003
LBGK	B	0.4979	0.5114	0.4919	0.5020	0.5025	0.5014	0.6367	0.6468	0.6138	0.9290	0.9549	0.8694
	R	0.5385	0.9117	0.4898	0.4987	0.5003	0.4971	0.6112	0.6907	0.5435	1.0709	1.4626	0.7884

small enough, *i.e.*, when the location is sufficiently away from the corners so the nonlinear term $\boldsymbol{u}\cdot\boldsymbol{\nabla}\boldsymbol{u}$ is sufficiently small. The result also suggests that, with U and Re fixed, the velocity field obtained by using the ELBE or LBGK scheme with the bounce-back boundary conditions will not converge when the resolution N increases. This is because τ increases linearly with N (cf. Eq. (23)), and for the single-relaxation-time collision models with the bounce-back boundary conditions, $\Delta = 12\nu^2 = 12(NU/\mathrm{Re})^2$ (cf. Eq. (19b)), therefore location where $\boldsymbol{u} = \boldsymbol{0}$ is satisfied will move further and further away from the last fluid nodes as N increases.

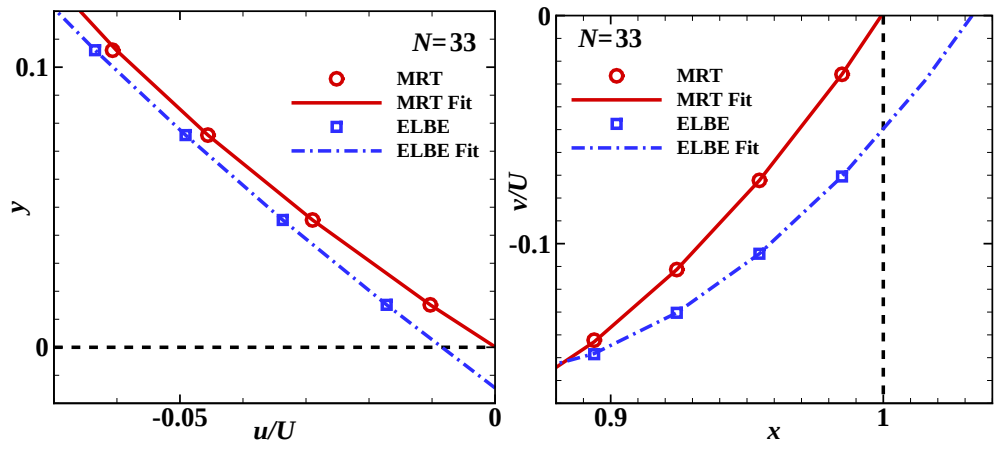

FIG. 10. (Color online) The tangential velocities near the bottom wall (left) and the right wall (right), $N^2 = 33^3$ and $\tau = 3.0$. The symbols are data obtained in simulations, and the dash-dot and solid lines correspond to Eqs. (30a) and (31), respectively. The straight dashed lines mark the assumed locations of the bottom wall $x = 0$ and the right wall $y = 1$.

To further substantiate this point, we compute the τ-dependence of the "slip" velocity $U_{\rm s}$ on the boundary node at the center of the bottom wall by using the ELBE scheme with $N = 33$. For a given value of τ, we can fit the velocity tangential to the wall with a parabola which includes two parameters: the effective maximum velocity U_* and the effective channel width N_*, as the results shown in Fig. 10. The velocity profile is then extrapolated to the boundary node to obtain the effective slip velocity $U_{\rm s}$, which is compared with the value of $U_{\rm s}$ computed from Eq. (30b). As shown in Fig. 11, clearly the τ-dependence of $U_{\rm s}/U_*$ in the cavity flow is well predicted by Eq. (30b), which is exact for the Poiseuille flow. Therefore, to achieve convergence by using the SRT-LB schemes, *i.e.*, the ELBE and LBGK schemes, with the bounce-back boundary conditions, one must maintain a constant ν with a fixed Re in order to control the error due to inaccurate boundary conditions, that means the product UN must be kept as a constant so U must decrease as $1/N$ when the resolution N increases. Consequently the number of iterations for the SRT-LB schemes to attain steady state would grow as $\mathrm{Re}N^2$, as opposed to $\mathrm{Re}N/U$ for the MRT-LB schemes with U kept as a constant.

Our results shown in Table IV and Figs. 10 and 11 unequivocally demonstrate that the so-called "slip velocity" $U_{\rm s}$ obtained by using the ELBE and LBGK schemes is merely a numerical artifact of these models due to their inaccurate boundary conditions. The "slip velocity" obtained by using any scheme based on the SRT model, such as the ELBE and

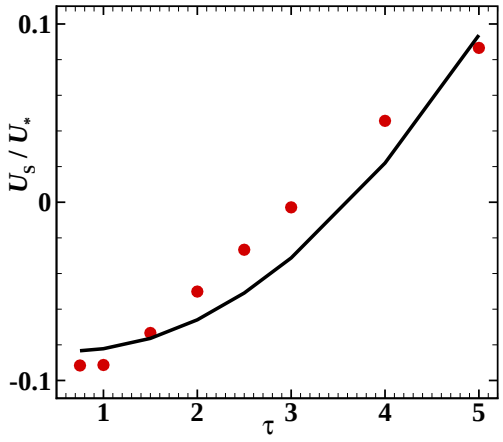

FIG. 11. (Color online) The τ-dependence of the tangential velocity U_s at the boundary node at the center of the bottom wall. $N^2 = 33^2$. The symbols and the solid line are data obtained by using the ELBE scheme and Eqs. (30a), respectively.

LBGK ones, cannot converge as N increases with fixed Re, Ma, and Kn, hence it is N dependent. In fact, for most ELBE and LBGK simulations of flow through a microchannel [35–37, 50], the resolution N is indeed used as a fitting parameter, and such results are erroneous and flawed, as pointed out previously [38, 39, 41, 51]. On the other hand, the MRT-LBE is free of the inherent defects of the SRT model, and is capable of reproducing convergent results [41].

D. Accuracy and Convergence

We now study the convergence behavior of the LB schemes. For the Reynolds number Re = 100, 400, and 1,000, the mesh resolutions, N^2, used for the LB simulations are: 65^2, 129^2, 257^2, and 513^2. We first compute the total energy E and the total enstrophy Z of the system:

$$E = \frac{\frac{1}{2}\int_\Omega \|\boldsymbol{u}(\boldsymbol{x})\|^2\, d\boldsymbol{x}}{\int_\Omega d\boldsymbol{x}} = \frac{\frac{1}{2}\sum_i \|\boldsymbol{u}(\boldsymbol{x}_i)\|^2}{N^2}\,, \tag{32a}$$

$$Z = \frac{\frac{1}{2}\int_\Omega \omega^2(\boldsymbol{x})\, d\boldsymbol{x}}{\int_\Omega d\boldsymbol{x}} = \frac{\frac{1}{2}\sum_i \omega^2(\boldsymbol{x}_i)}{N^2}\,, \tag{32b}$$

where Ω is the entire flow domain, and both the velocity $\boldsymbol{u}$ and the vorticity ω have been properly normalized by U and L/U, respectively. We also compute the L^2-normed error for the velocity field, $\boldsymbol{u}_N(\boldsymbol{x}_i)$, obtained by using an LB scheme with a given mesh resolution

N^2,

$$E_2(\boldsymbol{u}_N) := \frac{\sum_i \|\boldsymbol{u}_N(\boldsymbol{x}_i) - \boldsymbol{u}_*(\boldsymbol{x}_i)\|_2}{\sum_i \|\boldsymbol{u}_*(\boldsymbol{x}_i)\|_2}\,, \tag{33}$$

where $\boldsymbol{u}_*(\boldsymbol{x}_i)$ denotes the reference field. Two reference fields are used, the LB solution obtained with the largest mesh resolution of $N = 513$ and the PS-MG solution with $N = 96$. When the PS-MG solution is used as the reference solution, it is interpolated to the equispaced mesh of size N^2 used in the LB simulations. The above formula can also be applied to the vorticity and pressure fields. We can also estimate the convergence speed α as the following:

$$\alpha \approx \frac{\ln\left(E_2(\boldsymbol{u}_M)/E_2(\boldsymbol{u}_N)\right)}{\ln(N/M)}\,, \tag{34}$$

where $E_2(\boldsymbol{u}_M)$ and $E_2(\boldsymbol{u}_N)$ are the errors with the resolution M and N, respectively. In what follows, we will use the errors with two largest meshes to compute α.

When computing the total energy E and the total enstrophy Z, the integrations of $\boldsymbol{u}\cdot\boldsymbol{u}/2$ and $\omega^2/2$ are carried out over the entire flow domain Ω or only the fluid nodes, *i.e.*, excluding the boundary $\partial\Omega$. When the boundary $\partial\Omega$ is included in the integration, the integrand is weighted with a factor of $1/2$ and $1/4$ at $\partial\Omega$ and the four concerns, respectively, because the boundary is only $\delta_x/2$ away from the nearest fluid nodes. The Clenshaw-Curtis quadrature formula for integration is used to compute E and Z from the flow field obtained by using PS-MG method [18].

In Table V we present the total energy E integrated over Ω and $\Omega\backslash\partial\Omega$. Several observations can be made. First of all, the value of E computed on the entire flow domain Ω decreases monotonically as N increases, while the value of E computed on fluid nodes alone, *i.e.*, on $\Omega\backslash\partial\Omega$, increases monotonically, hence providing the upper and lower bounds of E, respectively. The lower and upper bounds obtained by the LB schemes with $N = 513$ have two or three significant digits agreeing with the PS-MG values, and the lower bounds are generally closer to the PS-MG values. This clearly indicates that the boundary conditions have considerable influence on the value of E. And second, the lower and upper bounds of E converge differently. The convergence speed for the upper bounds is about 1.0, independent of LB scheme, as showed by the left figure of Fig. 12. However, the convergence speed for the lower bounds is scheme-dependent. For the MRT-LB and TRT-LB schemes, the convergence speed is about 2.0; and the ELBE and LBGK schemes cease to converge when $N \geq 129$, as showed by the right figure of Fig. 12. This clearly indicates the importance of the boundary

conditions and demonstrates the superiority of the MRT-LB and TRT-LB schemes over the ELBE and LBGK schemes. The inaccuracy of the boundary conditions in the ELBE and LBGK schemes severely degrades the quality of the velocity field, as shown in the previous section, which in turn, negatively affect the quality of integral quantities in the system, such as E. Similar observation has made previously (cf., *e.g.*, [49]).

TABLE V. The total energy E on the entire flow domain Ω or only the interior, *i.e.*, the flow domain excluding the boundary $\Omega\backslash\partial\Omega$. The case of $N = 96$ is obtained by using the PS-MG method and the Clenshaw-Curtis quadrature formula for integration [18].

	E on Ω				E on $\Omega\backslash\partial\Omega$			
	MRT	TRT	ELBE	LBGK	MRT	TRT	ELBE	LBGK
N	Re = 100							
65	0.035838	0.035837	0.035968	0.036017	0.034173	0.034171	0.034311	0.034363
129	0.035223	0.035222	0.035185	0.035234	0.034371	0.034370	0.034332	0.034383
257	0.034855	0.034855	0.034770	0.034820	0.034424	0.034424	0.034337	0.034388
513	0.034655	0.034655	0.034556	0.034606	0.034438	0.034438	0.034338	0.034389
96	0.0344435487							
	Re = 400							
65	0.041307	0.041357	0.042193	0.042239	0.039983	0.040036	0.040925	0.040974
129	0.041299	0.041301	0.041444	0.041474	0.040637	0.040639	0.040786	0.040817
257	0.041108	0.041107	0.041111	0.041140	0.040774	0.040773	0.040778	0.040807
513	0.040972	0.040972	0.040945	0.040974	0.040804	0.040804	0.040778	0.040806
96	0.0408141964							
	Re = 1,000							
65	0.043148	0.043708	—	—	0.041939	0.042534	—	—
129	0.044602	0.044656	0.045221	0.045181	0.044043	0.044099	0.044681	0.044641
257	0.044704	0.044707	0.044861	0.044809	0.044426	0.044429	0.044586	0.044533
513	0.044638	0.044638	0.044711	0.044658	0.044499	0.044499	0.044573	0.044519
96	0.0445286399							

In Table VI we present the values of the total enstrophy Z computed over the entire fluid domain Ω or only on the fluid nodes $\Omega\backslash\partial\Omega$, similar to the total energy E in Table V. Because

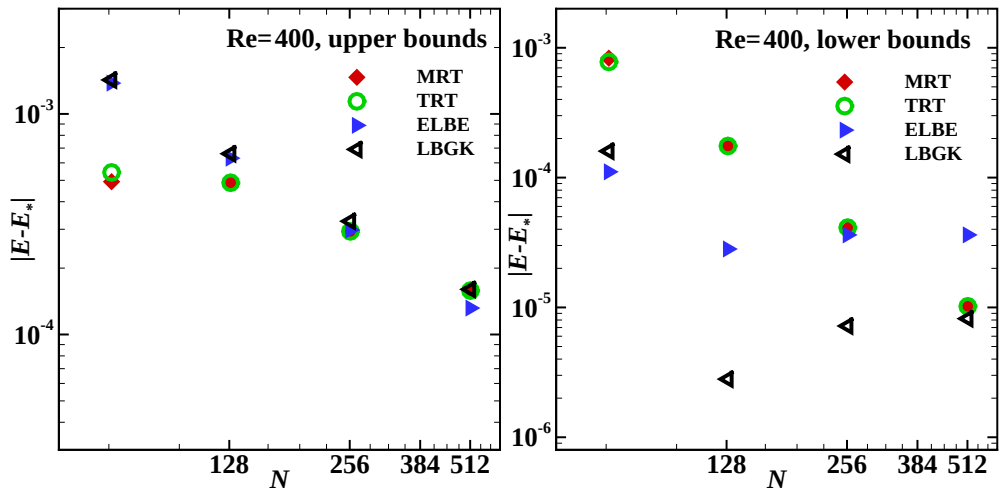

FIG. 12. (Color online) The convergence behaviors of the upper and lower bounds of the total energy E in Table V. Re = 400.

the vorticity $\omega = \boldsymbol{\nabla} \times \boldsymbol{u}$ is singular on the top corners, we should not expect ω computed with finite-difference to converge as N increases. Indeed, Z does not seem to converge when it is computed with the boundary value, while Z obtained by integrating over the fluid nodes alone appears to converge to the corresponding values obtained by using the PS-MG method with the convergence speed approximately equal to 1.0.

In Table VII we show the L^2-normed errors for the velocity field $\boldsymbol{u}$, the vorticity field ω, and the pressure field p, with the reference fields obtained by a particular LB scheme with the largest mesh size $N^2 = 513^2$. This is a consistency test to see if the solution of each LB scheme converges when mesh is refined. It should be pointed out that the grid points on two different meshes are not perfectly laying on top of each other because the boundary is only $\delta_x/2$ away from the fluid nodes adjacent to the boundary. This introduces a systematic error when it is assumed that the grid points on two meshes are perfectly aligned with each other. The alternative would be to interpolate data in one mesh to the grid points of the other mesh. This would introduce the error due to interpolations. We use the former approach, *i.e.*, assuming the grid points on two meshes are aligned with each other, because it is simpler. The data in Table VII shows that the convergence speed α for the velocity $\boldsymbol{u}$ and the vorticity ω is approximately 1.5 and 1.0, respectively, independent of the Reynolds number Re. As for the pressure p, the convergence speed depends not only on the Reynolds number Re, but also on the scheme. For the MRT-LB and TRT-LB schemes, the convergence

TABLE VI. The total enstrophy Z on the entire flow Ω or only the interior fluid nodes $\Omega\backslash\partial\Omega$. The case of $N = 96$ is obtained by using the PS-MG method [18].

	Z on Ω				Z on $\Omega\backslash\partial\Omega$			
	MRT	TRT	ELBE	LBGK	MRT	TRT	ELBE	LBGK
N	Re = 100							
65	13.871481	13.873742	13.454383	13.446956	9.269805	9.274383	9.241040	9.251079
129	15.482982	15.488585	15.427444	15.397035	10.750270	10.760709	10.739797	10.745891
257	17.029284	17.037512	17.887833	17.814132	12.230504	12.244964	12.430537	12.422978
513	18.530581	18.540718	21.699074	21.544143	13.700707	13.717798	14.644868	14.603368
96	17.4773036837							
	Re = 400							
65	17.742368	17.736531	16.868321	16.886885	11.825388	11.821156	12.095108	12.129003
129	19.037842	19.036509	18.393694	18.395769	13.470404	13.467743	13.525332	13.558239
257	20.300225	20.302552	19.875573	19.842928	15.017366	15.021890	14.965177	14.991985
513	21.604582	21.610247	21.598736	21.511861	16.510269	16.520684	16.491830	16.504690
96	20.2966851756							
	Re = 1,000							
65	23.821075	23.685784	—	—	15.291749	15.293886	—	—
129	24.687357	24.670743	23.508602	23.543192	17.348414	17.344816	17.595882	17.656577
257	25.466743	25.464046	24.721660	24.728690	19.089853	19.085165	19.169924	19.227861
513	26.384755	26.385888	25.887249	25.846128	20.662131	20.664337	20.606352	20.654849
96	24.4937074969							

speed for p increases from about 1.0 at Re = 100 to about 1.5 at Re = 1,000. For the ELBE and LBGK schemes, the trend is the opposite: the convergence speed decreases from about 1.5 at Re = 100 to about 1.0 at Re = 1,000. Given the singular nature of the flow, the convergence speeds for $\boldsymbol{u}$, ω, and p observed here are those of a second-order scheme and consistent with the theory [29].

In Table VIII we show the L^2-normed errors by using the PS-MG solutions with $N = 96$ [18] as the reference fields in Eq. (33). The errors are computed over the entire flow domain Ω, *i.e.*, including the boundary $\partial\Omega$. We note that the errors between the LB and PS-

TABLE VII. Convergence of the LB simulations. The reference fields in Eq. (33) are obtained by using the LB schemes with the largest mesh size $N^2 = 513^2$. For $\mathrm{Re} = 1,000$, both the ELBE and LBGK schemes are unstable when $N = 65$. The rows denoted with "α" are the convergence speed.

	$E_2(\boldsymbol{u})$				$E_2(\omega)$				$E_2(p)$			
	MRT	TRT	ELBE	LBGK	MRT	TRT	ELBE	LBGK	MRT	TRT	ELBE	LBGK
N	Re = 100											
65	0.086320	0.086237	0.075633	0.075838	0.813140	0.813394	0.806760	0.810152	0.823758	0.834287	0.585283	0.585244
129	0.038947	0.038782	0.033147	0.033222	0.595578	0.595863	0.602381	0.605486	0.622870	0.638575	0.347275	0.347390
257	0.013212	0.013132	0.011064	0.011084	0.294511	0.298272	0.330958	0.330293	0.300127	0.314486	0.132029	0.132087
α	1.55	1.56	1.58	1.58	1.01	0.99	0.86	0.87	1.05	1.02	1.39	1.39
	Re = 400											
65	0.100600	0.100410	0.088230	0.088508	0.797194	0.798397	0.796002	0.799037	0.663377	0.684981	0.594142	0.593535
129	0.043847	0.043818	0.040090	0.040255	0.571285	0.572026	0.568732	0.572676	0.407075	0.426939	0.345349	0.345294
257	0.014651	0.014628	0.013630	0.013693	0.275600	0.278278	0.277395	0.277874	0.160402	0.170074	0.124284	0.124413
α	1.58	1.58	1.55	1.55	1.05	1.03	1.03	1.04	1.34	1.32	1.47	1.47
	Re = 1,000											
65	0.124179	0.121146	—	—	0.782128	0.783456	—	—	0.457776	0.470430	—	—
129	0.051978	0.051735	0.046169	0.046380	0.544739	0.546456	0.565525	0.568647	0.230639	0.238365	0.338832	0.340169
257	0.017065	0.017048	0.016146	0.016222	0.256228	0.257526	0.280737	0.284390	0.081443	0.084864	0.153368	0.153689
α	1.60	1.60	1.51	1.51	1.08	1.08	1.01	0.99	1.50	1.48	1.14	1.14

MG solutions are smaller in general than those in Table VII, except some isolated cases: the velocity field $\boldsymbol{u}$ computed by using the ELBE scheme at Re = 400 and 1,000 and the pressure field at $\mathrm{Re} = 1,000$. This suggests that the systematic error due to mismatched grid points in the LB grid refinement may not be negligible. The convergence speed α for the velocity field obtained by using the MRT-LB and TRT-LB schemes weakly depends on the Reynolds number Re: it varies between 1.09 at Re = 100 and 1.30 at $\mathrm{Re} = 1,000$. In contrast, the convergence speed of the velocity field obtained by using the ELBE and LBGK schemes has a much stronger dependence on Re. For both the ELBE and LBGK schemes, at Re = 100 the velocity field fails to converge. At Re = 400 and 1,000, the ELBE scheme converges very slowly, while the LBGK scheme converges with a speed of about 1.5 or better. However, we can expect the convergence behavior of the ELBE and LBGK schemes to deteriorate as the mesh size N becomes sufficiently large so that $\tau > 1$, due to their inaccurate boundary conditions.

The vorticity field obtained by the LB schemes converges very slowly to the PS-MG solution, while the pressure field does not seem to converge at all. In absence of a body force, the vorticity $\boldsymbol{\omega}$ in compressible flows satisfies the following equation:

$$\partial_t \boldsymbol{\omega} + \boldsymbol{u}\cdot\boldsymbol{\nabla}\boldsymbol{\omega} = \boldsymbol{\omega}\cdot\boldsymbol{\nabla}\boldsymbol{u} - \boldsymbol{\omega}\boldsymbol{\nabla}\cdot\boldsymbol{u} + \frac{1}{\rho^2}\boldsymbol{\nabla}p\times\boldsymbol{\nabla}p + \boldsymbol{\nabla}\times\left(\frac{1}{\rho}\boldsymbol{\nabla}\cdot\sigma\right), \tag{35}$$

where σ is the stress tensor including the bulk viscosity ζ. For incompressible flows, $\boldsymbol{\nabla}\cdot\boldsymbol{u} = 0$,

TABLE VIII. Convergence of the LB simulations. The reference fields in Eq. (33) are obtained by using the PS-MG method with $N = 96$ collocation points in each dimension [18]. The PS-MG solutions are interpolated to the equispaced meshes used in the LB simulations. For the convergence speed α, "—" indicates the error not convergent, and "0" indicates very small α.

	$E_2(\boldsymbol{u})$				$E_2(\omega)$				$E_2(p)$			
N	MRT	TRT	ELBE	LBGK	MRT	TRT	ELBE	LBGK	MRT	TRT	ELBE	LBGK
	Re = 100											
65	0.009656	0.009596	0.013264	0.012407	0.404343	0.403632	0.405224	0.411644	0.139478	0.132741	0.130186	0.130833
129	0.004881	0.004762	0.006520	0.004521	0.349975	0.348526	0.341324	0.348427	0.142614	0.126274	0.108636	0.107584
257	0.002627	0.002536	0.007008	0.005103	0.312173	0.310392	0.309956	0.318039	0.139070	0.118188	0.210484	0.209649
513	0.001230	0.001159	0.008170	0.006575	0.278520	0.276377	0.317375	0.325069	0.133328	0.110153	0.294257	0.293612
α	1.09	1.12	—	—	0.16	0.16	—	—	0.06	0.10	—	—
	Re = 400											
65	0.014338	0.013976	0.032697	0.032139	0.537835	0.538175	0.577239	0.582646	0.059236	0.064428	0.552563	0.557939
129	0.005045	0.005046	0.011319	0.010116	0.434750	0.435049	0.450761	0.456535	0.060323	0.064410	0.215502	0.217022
257	0.002425	0.002412	0.005523	0.003001	0.358009	0.357551	0.356791	0.362463	0.065658	0.063101	0.063333	0.063627
513	0.001103	0.001076	0.004624	0.001022	0.299231	0.298099	0.292251	0.297964	0.067925	0.061149	0.054081	0.053463
α	1.13	1.16	0.25	0.28	0.25	0.26	0.28	0.28	—	0.045	0.22	0.25
	Re = 1,000											
65	0.034915	0.029041	—	—	0.646958	0.638229	—	—	0.185030	0.163602	—	—
129	0.008008	0.007549	0.018693	0.017704	0.521715	0.521236	0.550802	0.555590	0.160785	0.159536	0.364401	0.367965
257	0.002737	0.002726	0.007693	0.005767	0.416626	0.416986	0.433239	0.438302	0.158460	0.158936	0.206599	0.207348
513	0.001111	0.001108	0.005084	0.001694	0.333622	0.333426	0.335350	0.340138	0.158451	0.158393	0.162416	0.162488
α	1.30	1.29	0.59	1.53	0.32	0.32	0.36	0.36	0	0.0049	0.34	0.35

the density ρ is a constant, and the pressure p satisfies the Poisson equation. Since the LBE does not solve the Poisson equation accurately [29, 52], the compressibility effect can affect ω through all the terms involving $\boldsymbol{u}$, p, and σ in Eq. (35), for the velocity field $\boldsymbol{u}$ has a non-negligible dilatational component. It appears that the compressible effect in the LB solution severely degrades the accuracy of the vorticity field in this case. We will quantify the compressibility effect later.

To further investigate the convergence behavior of the LB schemes, we compute the differences between the flow fields obtained by the LB schemes and the PS-MG method in the middle portion of the interior flow domain, which excludes $(N-1)/32$ grids around the boundary, this reduces the total number of grid points by about $N^2 \times 31/256 \approx N^2/8$. As shown in Table IX, the errors in the interior are significantly smaller than their counterparts on the entire flow domain Ω except the following cases: the velocity field computed by using the ELBE scheme at Re = 400 and 1,000, the vorticity field by the ELBE and LBGK schemes at Re = 100, and the pressure field by all LB schemes at Re = 1,000. The convergence speed is also changed. Compared to the errors on the entire flow domain Ω, the convergence speed of the velocity field by using the MRT-LB and TRT-LB schemes has decreases slightly

to about 0.65 (from *ca.* 1.1), and has increases to about 1.68 and 1.81 (from *ca.* 1.13 and 1.30) at Re = 400 and 1,000, respectively. The convergence speed by using the ELBE scheme decreases to about 0.07 and 0.12 (from *ca.* 0.25 and 0.60) at Re = 400 and 1,000, respectively, while that by using the LBGK scheme decreases slightly to about 1.36 and 1.6 (from *ca.* 1.55 and 1.75).

TABLE IX. Convergence of the LB simulations, same as in Table VIII. The errors are computed over the interior flow domain by cutting away $(N-1)/32$ grid points along the boundary. For the convergence speed α, "—" indicates the error not convergent, and "0" indicates very small α.

	$E_2(\boldsymbol{u})$				$E_2(\omega)$				$E_2(p)$			
N	MRT	TRT	ELBE	LBGK	MRT	TRT	ELBE	LBGK	MRT	TRT	ELBE	LBGK
	Re = 100											
65	0.003252	0.003191	0.005719	0.004002	0.035406	0.037472	0.082058	0.083648	0.014485	0.014595	0.062072	0.062115
129	0.000779	0.000767	0.003543	0.000608	0.011840	0.012174	0.014103	0.013633	0.011412	0.011346	0.011463	0.011121
257	0.000238	0.000238	0.003459	0.000874	0.003290	0.003324	0.007181	0.001070	0.010858	0.010839	0.012035	0.011690
513	0.000152	0.000152	0.003462	0.001010	0.000868	0.000869	0.008341	0.003268	0.010733	0.010728	0.012277	0.011936
α	0.65	0.65	—	—	1.92	1.93	—	—	0.0016	0.0014	—	—
	Re = 400											
65	0.012047	0.011806	0.018762	0.017260	0.061100	0.055325	0.294266	0.297101	0.040048	0.038949	0.366186	0.368029
129	0.002522	0.002508	0.005850	0.001903	0.016072	0.015879	0.040473	0.039531	0.035796	0.035834	0.046303	0.045871
257	0.000577	0.000580	0.004789	0.000434	0.004224	0.004235	0.010929	0.005740	0.035835	0.035792	0.036286	0.035842
513	0.000180	0.000181	0.004563	0.000169	0.001107	0.001107	0.008579	0.001189	0.035868	0.035850	0.036271	0.035855
α	1.68	1.68	0.0069	1.36	1.93	1.93	0.34	2.27	—	—	0	—
	Re = 1,000											
65	0.034225	0.028946	—	—	0.114977	0.103268	—	—	0.191773	0.186110	—	—
129	0.006475	0.006042	0.007961	0.004135	0.028005	0.026225	0.133858	0.134461	0.178741	0.178870	0.210671	0.210918
257	0.001408	0.001388	0.005462	0.000653	0.006668	0.006636	0.016632	0.009163	0.178174	0.178190	0.178190	0.178197
513	0.000401	0.000402	0.005028	0.000215	0.001722	0.001722	0.012118	0.001900	0.178148	0.178144	0.178118	0.178141
α	1.81	1.78	0.11	1.60	1.95	1.94	0.45	2.26	0	0	0	0

The the convergence speed of ω on the interior flow domain is considerably better than that on the entire flow domain. It is particularly interesting to note that in many cases the convergence speed of the vorticity field ω in the interior flow domain is consistently better than that of the velocity field $\boldsymbol{u}$, as evidently shown in Table IX. For the MRT-LB and TRT-LB schemes, the convergence speed of ω is better than 1.9 in all cases, as opposed to between 0.16 and 0.32 on the entire flow domain. The ability of the MRT-LBE to accurately compute vorticity field has also been observed in simulations of turbulence in three dimensions [16]. For the LBGK scheme, the convergence speed of ω is better than 2.2 at Re = 400 and 1,000. As for the ELBE scheme, the convergence speed of ω is only 0.34 and 0.45 at Re = 400 and 1,000, respectively. As for the pressure field p, the convergence speed remains the same as on the entire flow domain — the pressure field does not appear to converge to the PS-MG solution.

The data in Table IX reveals some interesting observations. First, the error in the LB simulations concentrates mostly in the boundary region. In the case of the cavity flow, the corner singularities may be the main cause of the problem. And secondly, with carefully tuned equilibria, the MRT-LBE can solve both the velocity field $\boldsymbol{u}$ and vorticity field ω with a convergence speed about 2 in regions where the flow is smooth. This can be explained as the following. According to Noether's theorem, which states that any differentiable symmetry of the action of a physical system has a corresponding conservation law, the conservation laws of the linear and angular momenta correspond to Galilean and rotational invariance, respectively. The LBE preserves both invariances up to second order in the wavevector $\boldsymbol{k}$ [9], and consequently the conservation laws of the linear and angular momenta to the same order of accuracy. Although this does not constitute a rigorous proof, it helps explain the phenomenon.

With $\mathrm{Ma} = 0.1 \times \sqrt{3} \approx 0.1732$, the rms density fluctuation $\sqrt{\langle \delta\rho^2 \rangle}$ in the system is of the order $O(10^{-3})$ (cf. Table X related discussion later). Given the fact that the pressure field p obtained by using the LB schemes has a significant compressibility component proportional to Ma^2, it is expected that the pressure p is most sensitive to the error due to the compressibility effect in the LBE. The data in Table IX attests again the crucial role of the boundary conditions play in the LB simulations. Clearly the MRT-LB and TRT-LB schemes are far more accurate than the ELBE and LBGK schemes in terms of the convergence speed and the magnitude of errors in $\boldsymbol{u}$ and ω, and the ELBE scheme is the most inferior in all these measures.

To quantify the compressibility effect, we compute the root-mean-square (rms) density fluctuation $\sqrt{\langle (\delta\rho)^2 \rangle}$ and the rms velocity divergence $\sqrt{\langle (\boldsymbol{\nabla}\cdot\boldsymbol{u})^2 \rangle}$ in the system:

$$\sqrt{\langle (\delta\rho)^2 \rangle} = \left[\frac{\sum_i (\delta\rho)^2(\boldsymbol{x}_i)}{N_x \times N_y} \right]^{1/2}, \tag{36a}$$

$$\sqrt{\langle (\boldsymbol{\nabla}\cdot\boldsymbol{u})^2 \rangle} = \left[\frac{\sum_i (\boldsymbol{\nabla}\cdot\boldsymbol{u})^2(\boldsymbol{x}_i)}{N_x \times N_y} \right]^{1/2}, \tag{36b}$$

where $\boldsymbol{x}_i$ are fluid nodes. The results of $\sqrt{\langle (\delta\rho)^2 \rangle}$ and $\sqrt{\langle (\boldsymbol{\nabla}\cdot\boldsymbol{u})^2 \rangle}$ are tabulated in Table X.

Several observations can be made. First of all, for all LB schemes, with a fixed the Mach number Ma, the rms density fluctuation $\sqrt{\langle (\delta\rho)^2 \rangle}$ is nearly independent of the mesh resolution N and decreases as the Reynolds number Re increases. The rms density fluctuation is approximately equal to 3.0×10^{-3}, 1.6×10^{-3}, and 1.3×10^{-3}, at $\mathrm{Re} = 100$, 400, and 1,000,

respectively.

And secondly, for the MRT-LB and TRT-LB schemes, the rms velocity divergence $\sqrt{\langle(\boldsymbol{\nabla}\cdot\boldsymbol{u})^2\rangle}$ does not seem to depend on either N or Re. As for the ELBE and LBGK schemes, the rms velocity divergence decreases as N increases, and increases as Re increases. Since in the ELBE and LBGK schemes the bulk viscosity $\zeta = \nu/2$, as Re increases with a fixed N, ζ decreases, and so similarly do the decay rates of all other non-conserved modes, leading to weaker dissipation to all non-conserved modes, including the modes related to the compressibility term $\boldsymbol{\nabla}\rho\zeta\boldsymbol{\nabla}\cdot\boldsymbol{u}$ in the Navier-Stokes equation. In the case of increasing N with a fixed Re, ζ and all the other decay rates increase, resulting in stronger dissipation to the modes related to the compressibility effect. This explains the dependence of the rms velocity divergence on N and Re for the ELBE and LBGK schemes. It is interesting to note that the bulk viscosity ζ in the MRT-LBE is fixed, while in the TRT-LBE it is identical to that in the LBGK scheme, and yet, the rms density fluctuation and the rms velocity divergence behave almost identically for the MRT-LB and TRT-LB schemes. This indicates that the dissipation of the "heat fluxes" $\boldsymbol{q}$, determined by s_q, and the boundary conditions play a crucial role here. This is certainly more complicated than the case without boundary [23], and suggests that the TRT-LBE is a much better approach than the ELBE with a tunable bulk viscosity [26].

Finally, since the rms density fluctuation and the rms velocity divergence are the direct measures of the compressibility effect, which is proportional to $O(\mathrm{Ma}^2)$, and the pressure field is most direly affect by the compressibility effect through the simple equation of state in the LBE, $p = c_s^2\rho$, thus, to improve the accuracy of the pressure field p, the Mach number must be decreased, as observed previously (cf. [23, 43]).

E. Stability and computational efficiency

To compare the numerical stability of the LB schemes, we conduct the following test. With a small mesh size $N^2 = 17^2$ and a given value of the viscosity ν, we search the maximum lid velocity U such that the simulation does not diverge with 1,000 iterations. For the MRT-LBE, in addition to $s_\nu = 1/\tau$, there are three adjustable relaxation rates: s_q, s_e, and s_ϵ. To accurately realize the no-slip boundary conditions through the bounce-back boundary conditions, s_q must be a fixed function of s_ν (cf. Eq. (11)). However, to

TABLE X. The dependence of the rms density fluctuation $\sqrt{\langle(\delta\rho)^2\rangle}$ and the rms velocity divergence $\sqrt{\langle(\boldsymbol{\nabla}\cdot\boldsymbol{u})^2\rangle}$ on the Reynolds number Re and the mesh size N.

	rms density fluctuation				rms velocity divergence			
N	MRT	TRT	ELBE	LBGK	MRT	TRT	ELBE	LBGK
	Re = 100							
65	0.002569	0.002574	0.002850	0.002855	0.305216	0.302737	0.360637	0.361507
129	0.002753	0.002764	0.002789	0.002793	0.305982	0.299739	0.309758	0.310092
257	0.002926	0.002940	0.002803	0.002806	0.309262	0.298951	0.241936	0.239084
513	0.003091	0.003105	0.002822	0.002826	0.313143	0.298658	0.191387	0.181124
	Re = 400							
65	0.001533	0.001530	0.001898	0.001905	0.321806	0.329121	0.530087	0.528835
129	0.001564	0.001563	0.001670	0.001672	0.310099	0.311752	0.426615	0.428021
257	0.001586	0.001587	0.001618	0.001619	0.305285	0.302858	0.359677	0.362329
513	0.001607	0.001608	0.001610	0.001611	0.305859	0.299648	0.308708	0.310513
	Re = 1,000							
65	0.001321	0.001329	—	—	0.345939	0.359265	—	—
129	0.001368	0.001368	0.001491	0.001491	0.325027	0.334810	0.567532	0.567025
257	0.001379	0.001379	0.001413	0.001411	0.313045	0.316334	0.456678	0.458426
513	0.001384	0.001384	0.001396	0.001394	0.305985	0.304804	0.375882	0.379374

demonstrate the effect of s_q on the numerical stability of the MRT-LBE, we also vary s_q independently in the test. Table XI lists the values of relaxation rates used in the test.

In Fig. 13 we show the result of the stability test. Clearly, the ELBE and LBGK schemes are shown to be the most inferior in this test, and there is no observable difference between the ELBE and LBGK schemes in terms of stability. It is evident that the ELBE scheme does not improve numerical stability of the LBGK scheme. The TRT-LB scheme is more stable than both the ELBE and LBGK schemes. By far, the MRT-LBE is the most stable scheme. However, as the viscosity ν decreases, the stability of the MRT-LB scheme deteriorate considerably. As $s_\nu = 1/\tau$ approaches to 2, $s_q(s_\nu)$ approaches to 0, the relaxation time of the modes q_x and q_y becomes longer and longer, so that q_x and q_y become quasi-conserved modes eventually when s_q is sufficiently small. This apparently affects the stability of the

TABLE XI. The values of the relaxation rates used in the stability test shown in Fig. 13.

Model	Relaxation Rates		
	s_e	s_ϵ	s_q
MRT	1.64	1.54	$8(2\tau-1)/(8\tau-1)$
MRT1	1.64	1.54	1.9
MRT2	1.8	1.54	1.9
MRT3	1.64	1.8	1.9
MRT4	$1/\tau$	1.9	$8(2\tau-1)/(8\tau-1)$
TRT	$1/\tau$	$1/\tau$	$8(2\tau-1)/(8\tau-1)$

MRT-LBE when $s_\nu = 1/\tau$ is close to 2. If s_q is fixed at 1.9 or so while other relaxation rates are unchanged (corresponding to MRT1 in Table XI and Fig. 13), then the stability of the MRT-LBE is improved when $s_\nu = 1/\tau \gtrsim 1.965$, but degraded when $s_\nu = 1/\tau \lesssim 1.965$, as shown in Fig. 13. If we use $s_q = 1.9$ and increase s_e from 1.64 to 1.8 (the case MRT2 in Fig. 13), the stability is weaker than the case of MRT1.

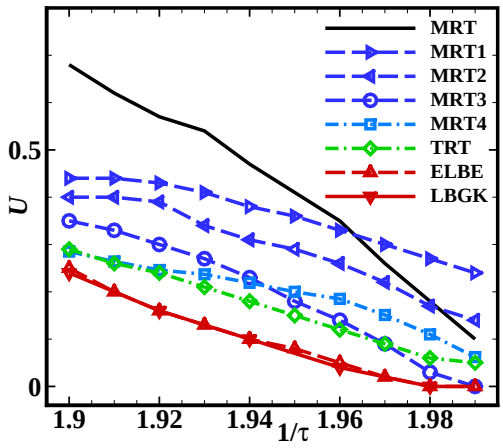

FIG. 13. (Color online) The stability characteristics of various LBE models. $N^2 = 17^2$. The test is deemed stable if it does not diverge within 1,000 iterations.

We note that the numerical stability of the LBE can be affected by factors other than the relaxation rates. For example, the stability would be different if one uses the "compressible" version of the LBGK model of which the equilibria are [53]:

$$f_i^{(\mathrm{eq})} = w_i\,\rho\left[1+\frac{\boldsymbol{c}_i\cdot\boldsymbol{u}}{c_s^2}+\frac{1}{2}\left\{\frac{(\boldsymbol{c}_i\cdot\boldsymbol{u})^2}{c_s^4}-\frac{\boldsymbol{u}\cdot\boldsymbol{u}}{c_s^2}\right\}\right]. \tag{37}$$

We do not use the "compressible" LB model because we would like to minimize the compressibility effect, because we are only interested in simulating incompressible flows. Another factor may be the mean density ρ_0. In our implementation, we set $\rho_0 = 1$ so the LBE can approximate the Poisson equation obeyed by the pressure [52]. In addition, to reduce the effects due to round-off error we only consider the density fluctuation $\delta\rho$ in the mass conservation [22, 23], as indicated in the equilibria defined by Eqs. (5) and (12). With a value of $\rho_0 > 1$ [53], the effect of the round-off error is enhanced, but the relative density fluctuation $\delta\rho/\rho_0$ is reduced, hence the stability might be improved.

We should also emphasize that the numerical stability must be discussed in connection with accuracy and computational efficiency. That is, one must not pursue stability at the expense of accuracy and efficiency, and especially accuracy. To optimize the computational efficiency, U should be maximized, for a larger U effectively leads to a larger CFL number, as discussed previously in Sec. III A. However, the truncation error due to $\boldsymbol{u}^3$ terms grow as U increases [9], which can be eliminated only with a larger discrete velocity set, *e.g.*, D2Q21 model [54]. With these considerations in mind, one should use the maximal value of U without compromising accuracy. With U properly chosen, the issue of optimizing the stability becomes minimizing the viscosity ν. However, one should not relentlessly push the lower limit of ν, otherwise the results of direct numerical simulations become dubious if the grid Reynolds number $\mathrm{Re}^* := U\delta_x/\nu$ becomes too large. Thus, one must strike a balance between accuracy, efficiency, and stability, and in that order.

To compare computational speed of different LB schemes, we use a mesh of size $N^2 = 129^2$ with the Reynolds numbers $\mathrm{Re} = 1,000$, 1,500, 1,800, and 2,000. All the computations are carried out on an Intel Xeon (x86-64) processor with two dual core of 2.992GHz and 8GB RAM. The codes are written in C and compiled with the Intel compiler icpc. Table XII provides the number of iterations (N_t) and the CPU times (T_{CPU}) for the LB schemes to attain a steady state according to the criterion of Eq. (21), and the ratios (R_{T}) between the CPU times of the MRT, TRT, and ELBE schemes *versus* the LBGK scheme, of which the CPU time is the shortest. Clearly we can see in Table XII that the number of iterations to reach steady state $N_t \propto N\mathrm{Re}/U$. The results also show that, while the TRT-LB and MRT-LB schemes are about 15% and 25% slower than the LBGK scheme in terms of CPU time, respectively, the ELBE scheme is about 2.5 times slower. We also note that with the mesh size of $N^2 = 129^2$, both the ELBE and LBGK do not converge for $\mathrm{Re} = 2,000$.

TABLE XII. The number of iterations N_t and CPU time $T_{\rm CPU}$ (seconds) for different LB schemes to attain the steady state with different values of the Reynolds number Re. $N^2 = 129^2$. The numbers in parentheses () are the ratio $R_{\rm T}$ of the CPU times of the TRT, MRT, and ELBE schemes *vs.* that of the LBGK scheme. "—" indicates the simulation does not converge.

Re	1,000			1,500			1,800			2,000	
	N_t	$T_{\rm CPU}$	$R_{\rm T}$	N_t	$T_{\rm CPU}$	$R_{\rm T}$	N_t	$T_{\rm CPU}$	$R_{\rm T}$	N_t	$T_{\rm CPU}$
LBGK	413,000	194.12	(1)	645,000	296.11	(1)	785,000	354.63	(1)	—	
TRT	413,000	217.77	(1.12)	643,000	338.75	(1.14)	782,000	413.48	(1.17)	874,000	460.34
MRT	413,000	235.96	(1.22)	645,000	366.74	(1.24)	785,000	443.76	(1.25)	878,000	498.29
ELBE	415,000	491.39	(2.53)	648,000	766.60	(2.59)	790,000	930.06	(2.62)	—	

IV. CONCLUSIONS AND DISCUSSION

In this work we conduct a comparative study of several lattice Boltzmann schemes including the MRT-LB, TRT-LB, ELBE, and LBGK D2Q9 models, in terms of accuracy, numerical stability, and computational efficiency. As a benchmark test, we use the lid-driven square cavity flow in 2D with the Reynolds numbers Re = 100, 400, and 1,000, for which the flow is steady and laminar. We compare the LB solutions with the solutions obtained by using the pseudo-spectral multigrid method with singularity subtraction technique [18]. The evidence shows that the MRT-LB and TRT-LB schemes are superior over the ELBE and LBGK schemes in terms of accuracy, stability, and computational efficiency.

We made the following observations through this study. First, all the LB schemes are capable of capturing the gross hydrodynamic features of the flow. We compare the contours of the pressure field p, the stream function ψ, and the vorticity field ω computed by using the LB schemes with those by using the PS-MG method [18], and find that they agree well with each other. The LB schemes can reproduce quantitatively accurate results, such as the locations and intensities of the primary, secondary, and even tertiary vortexes. Both the MRT-LB and the TRT-LB schemes can capture the tertiary vortex at Re $= 1,000$ with a mesh of size $N^2 = 129^2$, while both the ELBE and LBGK schemes require a finer mesh of size $N^2 = 257^2$ to observe the tertiary vortex.

Second, we observe that one major source of errors in the LB simulations comes from boundary conditions, and this problem is particularly severe for the ELBE and LBGK

schemes coupled with the bounce-back boundary conditions. The problem is two-fold: with the relaxation parameter τ close to 1/2, flow fields near no-slip boundaries oscillate severely with high frequencies, and with $\tau \gg 1$, the boundary locations move away from supposed positions considerably and are τ-dependent. Both these defects can be overcome by using the MRT models.

Third, all the LB schemes (MRT, TRT, ELBE, and LBGK) exhibit a self-consistent convergence behavior of a second-order scheme, as expected [29]. The solutions of the velocity $\boldsymbol{u}$, the vorticity ω, and the pressure p obtained by using a particular LB scheme converge to unique limiting states as the resolution N increases with expected convergence speed. However, the LB solutions of $\boldsymbol{u}$, ω, and p do not necessarily converge to the corresponding solutions of the pseudo-spectral method [18]. When compared with the PS solution of the velocity field $\boldsymbol{u}$ on the entire flow domain, both the MRT-LB and TRT-LB schemes are shown to be only marginally of second-order convergence, so is the LBGK scheme at $Re = 1,000$, while the ELBE scheme is only of first-order. However, when compared with the PS solution of the velocity field $\boldsymbol{u}$ in the interior flow domain, the MRT-LB, TRT-LB, and LBGK schemes are clearly of second-order convergence, and the ELBE scheme is only of first-order convergence, excepted for the case of $Re = 100$. At $Re = 100$, both the MRT-LB and TRT-LB schemes are of first-order convergence, while neither the ELBE scheme nor the LBGK scheme converges at all. In particular, it is interesting to note that the vorticity field obtained by using the MRT-LB and TRT-LB schemes, and the LBGK scheme in some cases, is of second-order convergence, and the convergence speed is consistently better than that of the velocity field, while the convergence speed for the ELBE is only of first-order. In most cases, the pressure field p obtained by the LB schemes either converges very slowly or does not converge at all to the PS solution.

Fourth, we note that the ELBE scheme does not in anyway improve the stability of the LBGK scheme, while its computational cost is almost tripled. In terms of accuracy, the ELBE scheme is even inferior to the LBGK scheme. One reason that the ELBE cannot improve the stability is that, when τ is approaching 1/2, the ELBE does not have sufficient dissipation to damp density fluctuations in the system [9], and the interactions of the acoustic waves generated by density fluctuations can instigate numerical instabilities. To overcome this shortcoming of the ELBE scheme, an adjustable bulk viscosity can be introduced [26]. This approach basically adopts the MRT technique, but only half-heartily, while clinging to

all other deficiencies inherent to the ELBE/SRT methodology. We do not test the ELBE with a variable relaxation time [53, 55] which is supposed to guarantee numerical stability, because it is computationally inefficient and unphysical with a viscosity depending on space and time — a stable but inaccurate, unphysical, and inefficient scheme is simply not a viable one.

Fifth, in terms of CPU time the LBGK scheme is only about 25% and 15% faster than the MRT and TRT schemes, respectively. However, given the inherent deficiencies in the LBGK scheme, this insignificant saving in CPU time is besides the point, because the LBGK scheme with the bounce-back boundary conditions cannot yield convergent results as the mesh size N increases. Furthermore, for most LB algorithms which are light in floating point operations (FLOP), the computational speed is limited by memory bandwidth and cache size, thus the difference in the computational speed due to insignificantly different number of FLOP will diminish. Thus, 25% difference in CPU time is not a valid justification to use the LBGK scheme.

Finally, we would like to discuss the choice of the relaxation rates $\{s_i\}$ in the MRT-LBE. Often, critics of the MRT methodology complain its "complexity," and one aspect of the complexity is that it appears no analytic guidelines to determine the relaxation rates. These criticisms are not entirely valid. First of all, the MRT collision model is a *linear* one, of which the LBGK model is a special case, and it is well understood in kinetic theory and there exists a vast literature on the subject (cf., *e.g.*, [21] and references therein).

Within the context of the LBE, certain guidelines do exist. In kinetic theory, hydrodynamic time scales of the conserved modes are vastly separated from those of kinetic (non-conserved) modes, that is, time scales of kinetic (non-conserved) modes are much shorter than the hydrodynamic ones. This vast separation of time scales is not satisfied in the LBE for it has very limited number of modes which are closely coupled together through relative simple algebraic relationships defined by the LBE (2), so the range of these relaxation rates is rather limited, and the dynamics of kinetic modes in the LBE has severe effects on boundary conditions and numerical stability. It is difficult to determine, analytically and *a priori*, optimal relaxation rates in terms of both accuracy and stability. This is especially true for 3D models with a large number of discrete velocities (or the moments).

While it is relatively easy to obtain relaxation rates for optimal *linear* stability [9], it is not so for *nonlinear* stability. It is also not easy to analytically determine the effects of

relaxation rates on the boundary conditions in general (cf. [14]). However, one can still determine the relaxation rates which can be used to yield reasonable accuracy and stability. In this regard, the TRT-LBE is the simplest alternative which improves both accuracy and numerical stability. The point to emphasize is that the MRT formalism allows improvements by adjusting the relaxation rates, which is not possible for the models with single relaxation time. We note that a thorough and detailed investigation of the effects of the relaxation rates on the accuracy and stability is beyond the scope of this work and should be a subject of future studies.

The results of this study demonstrate that there are at least three relaxation rates, s_ν, s_q, and s_e, which have significant effects on accuracy and numerical stability of the MRT-LBE. Therefore, to optimize accuracy and numerical stability, it is necessary to have three adjustable degrees of freedom in the MRT-LBE provided by s_ν, s_q, and s_e, which determine the value of the shear viscosity ν (or the Reynolds number Re), the accurate locations of the Dirichlet boundary conditions, and the bulk viscosity ζ (cf. Eq. (10b)). If numerical stability is not a consideration, one should use the TRT-LBE [5–7], that is, the odd-order moments are relaxed by the rate $s_q(s_\nu)$ (cf. *e.g.*, Eq. (11) and [14, 56] and references therein), while the even-order moments are relaxed with the rate s_ν. With three adjustable relaxation rates, the MRT-LBE provides minimal degrees of freedom required by accuracy and stability, and can enhance the computational efficiency ultimately.

In summary, our conclusion is that, while it may be theoretically interesting, the ELBE scheme is so inferior to the MRT scheme in terms of accuracy, numerical stability, and computational efficiency that it must not be used as a practical scheme for numerical simulations. We also note that one important and challenging issue in the LBE is to improve accuracy of the pressure field p. In this regard, investigation of the artificial compressibility method [31, 32] may offer some new insights.

ACKNOWLEDGMENTS

This work is supported by the National Science Foundation (NSF) of the US through the Grant DMS-0807983. LSL would like to acknowledge the support of the Richard F. Barry Jr. endowment at the Old Dominion University (ODU). XWC would like to acknowledge the generous support of the Modeling and Simulation Scholarship provided by ODU during 2008

– 2010. This paper was written when LSL was a visiting fellow at Isaac Newton Institute of Mathematical Sciences, University of Cambridge, UK, August 16 – October 30, 2010.

---

[1] R. Mei, D. Yu, W. Shyy, L.-S. Luo, Force evaluation in the lattice Boltzmann method involving curved geometry, Phys. Rev. E 65 (2002) 041203.

[2] L.-S. Luo, M. Krafczyk, W. Shyy, Lattice Boltzmann method for computational fluid dynamics, in: R. Blockley, W. Shyy (Eds.), Encyclopedia of Aerospace Engineering, Wiley, New York, 2010, Ch. 56, pp. 651–660.

[3] S. Ansumali, I. V. Karlin, H. C. Öttinger, Minimal entropic kinetic models for hydrodynamics, Europhys. Lett. 63 (6) (2003) 798–804.

[4] S. Succi, I. V. Karlin, H. Chen, Role of the H theorem in lattice Boltzmann hydrodynamic simulations, Rev. Mod. Phys. 74 (2002) 1203–1220.

[5] I. Ginzburg, Equilibrium-type and link-type lattice Boltzmann models for generic advection and anisotropic-dispersion equation, Adv. Water Res. 28 (11) (2005) 1171–1195.

[6] I. Ginzburg, F. Verhaeghe, D. d'Humières, Two-relaxation-time lattice Boltzmann scheme: About parametrization, velocity, pressure and mixed boundary conditions, Commun. Comput. Phys. 3 (2) (2008) 427–478.

[7] I. Ginzburg, F. Verhaeghe, D. d'Humières, Study of simple hydrodynamic solutions with the two-relaxation-times lattice Boltzmann scheme, Commun. Comput. Phys. 3 (3) (2008) 519–581.

[8] D. d'Humières, Generalized lattice-Boltzmann equations, in: B. D. Shizgal, D. P. Weave (Eds.), Rarefied Gas Dynamics: Theory and Simulations, Vol. 159 of Prog. Astronaut. Aeronaut., AIAA, Washington, D.C., 1992, pp. 450–458.

[9] P. Lallemand, L.-S. Luo, Theory of the lattice Boltzmann method: Dispersion, dissipation, isotropy, Galilean invariance, and stability, Phys. Rev. E 61 (6) (2000) 6546–6562.

[10] D. d'Humières, I. Ginzburg, M. Krafczyk, P. Lallemand, L.-S. Luo, Multiple-relaxation-time lattice Boltzmann models in three-dimensions, Philos. Trans. R. Soc. Lond. A 360 (1792) (2002) 437–451.

[11] P. Lallemand, L.-S. Luo, Theory of the lattice Boltzmann method: Acoustic and thermal properties in two and three dimensions, Phys. Rev. E 68 (3) (2003) 036706.

[12] X. He, L.-S. Luo, A priori derivation of the lattice Boltzmann equation, Phys. Rev. E 55 (6) (1997) R6333–R6336.

[13] X. He, L.-S. Luo, Theory of lattice Boltzmann method: From the Boltzmann equation to the lattice Boltzmann equation, Phys. Rev. E 56 (6) (1997) 6811–6817.

[14] I. Ginzburg, D. d'Humières, Multireflection boundary conditions for lattice Boltzmann models, Phys. Rev. E 68 (6) (2003) 066614.

[15] C. Pan, L.-S. Luo, C. Miller, An evaluation of lattice Boltzmann schemes for porous medium flow simulation, Comput. Fluids 35 (8/9) (2006) 898–909.

[16] Y. Peng, W. Liao, L.-S. Luo, L.-P. Wang, Comparison of the lattice Boltzmann and pseudo-spectral methods for decaying turbulence. Low order statistics, Comput. Fluids 39 (4) (2010) 568–591.

[17] O. Botella, R. Peyret, Benchmark spectral results on the lid-driven cavity flow, Comput. Fluids 27 (4) (1998) 421–433.

[18] W. Zhang, C. Zhang, G. Xi, An explicit Chebyshev pseudospectral multigrid method for incompressible Navier-Stokes equations, Comput. Fluids 39 (1) (2010) 178–188.

[19] L.-S. Luo, Some recent results on discrete velocity models and ramifications for lattice Boltzmann equation, Comp. Phys. Commun. 129 (2000) 63–74.

[20] Y. Qian, D. d'Humières, P. Lallemand, Lattice BGK models for Navier-Stokes equation, Europhys. Lett. 17 (6) (1992) 479–484.

[21] S. Harris, An Introduction to the Theory of Boltzmann Equation, Holt, Rinehart and Winston, New York, 1971, reprinted by Dover, 2004.

[22] X. He, L.-S. Luo, Lattice Boltzmann model for the incompressible Navier-Stokes equation, J. Stat. Phys. 88 (3/4) (1997) 927–944.

[23] P. Dellar, Incompressible limits of lattice Boltzmann equations using multiple relaxation times, J. Comput. Phys. 190 (2) (2003) 351–370.

[24] I. Ginzbourg, Boundary conditions problems in lattice gas methods for single and multiple phases, Ph.D. thesis, Universite Paris VI, France (1994).

[25] I. Ginzbourg, P. M. Adler, Boundary flow condition analysis for the three-dimensional lattice Boltzmann model, J. Phys. II 4 (2) (1994) 191–214.

[26] P. Asinari, I. V. Karlin, Quasiequilibrium lattice Boltzmann models with tunable bulk viscosity for enhancing stability, Phys. Rev. E 81 (1) (2010) 016702.

[27] W.-A. Yong, L.-S. Luo, Nonexistence of H theorems for the athermal lattice Boltzmann models with polynomial equilibria, Phys. Rev. E 67 (2003) 051105.

[28] W.-A. Yong, L.-S. Luo, Nonexistence of H theorem for some lattice Boltzmann models, J. Stat. Phys. 121 (1/2) (2005) 91–103.

[29] M. Junk, A. Klar, L.-S. Luo, Asymptotic analysis of the lattice Boltzmann equation, J. Comput. Phys. 210 (2) (2005) 676–704.

[30] L. Saint-Raymond, Hydrodynamic Limits of the Boltzmann Equation, Vol. 1971 of Lecture Notes in Mathematics, Springer, Heidelberg, Germany, 2009.

[31] P. Asinari, V. Karlin, Connection between kinetic methods for fluid-dynamic equations and macroscopic finite-difference schemes, Comput. Math. Appl. 58 (5) (2009) 841–861.

[32] T. Ohwada, P. Asinari, Artificial compressibility method revisited: Asymptotic numerical method for incompressible Navier-Stokes equations, J. Comput. Phys. 229 (5) (2010) 1698–1723.

[33] L.-S. Luo, Analytic solutions of linearized lattice Boltzmann equation, J. Stat. Phys. 88 (3/4) (1997) 913–926.

[34] X. He, Q. Zou, L.-S. Luo, M. Dembo, Analytic solutions and analysis on non-slip boundary condition for the lattice Boltzmann BGK model, J. Stat. Phys. 87 (1/2) (1997) 115–136.

[35] S. Ansumali, I. Karlin, C. Frouzakis, K. Boulouchos, Entropic lattice Boltzmann method for microflows, Physica A 359 (2006) 289–305.

[36] Y. Zhou, R. Zhang, I. Staroselsky, H. Chen, W. Kim, M. Jhon, Simulation of micro- and nano-scale flows via the lattice Boltzmann method, Physica A 362 (1) (2006) 68–77.

[37] J. Ghazanfarian, A. Abbassi, Heat transfer and fluid flow in microchannels and nanochannels at high Knudsen number using thermal lattice-Boltzmann method, Phys. Rev. E 82 (2) (2010) 026307.

[38] C. Shen, D. B. Tian, C. Xie, J. Fan, Examination of the LBM in simulation of microchannel flow in transitional regime, Microscale Thermophys. Eng. 8 (4) (2004) 423–432.

[39] L.-S. Luo, Comment on "Discrete Boltzmann equation for microfluidics", Phys. Rev. Lett. 92 (13) (2004) 139401.

[40] R. Rubinstein, L.-S. Luo, Theory of the lattice Boltzmann equation: Symmetry properties of discrete velocity sets, Phys. Rev. E 77 (3) (2008) 036709.

[41] F. Verhaeghe, L.-S. Luo, B. Blanpain, Lattice Boltzmann modeling of microchannel flow in slip flow regime, J. Comput. Phys. 228 (1) (2009) 147–157.

[42] U. Ghia, K. N. Ghia, C. T. Shin, High-Re solutions for incompressible flow using the Navier-Stokes equations and a multigrid method, J. Comput. Phys. 48 (3) (1982) 387–411.

[43] S. L. Hou, Q. Zou, S. Chen, G. D. Doolen, A. C. Cogley, Simulation of cavity flow by the lattice Boltzmann method, J. Comput. Phys. 118 (1995) 329–347.

[44] P. Shankar, M. Deshpande, Fluid mechanics in the driven cavity, Annu. Rev. Fluid Mech. 32 (2000) 93–136.

[45] C.-H. Bruneau, M. Saad, The 2D lid-driven cavity problem revisited, Comput. Fluids 35 (3) (2006) 326–348.

[46] The CFL condition requires that $U < \Delta x/\Delta t$, where U is the characteristic velocity of the flow, and Δx and Δt are the grid spacing and the time step size, respectively, both of which are free parameters to be chosen. For the LBE, the incompressibility condition requires that $U/c_s < \mathrm{Ma}_*$, where $\mathrm{Ma}_* \approx 0.3$ is the approximate upper bound of the Mach number, *i.e.*, $U < (\mathrm{Ma}_*/\sqrt{3})\delta_x/\delta_t$. Therefore, the Mach number limit in the LBE can be seen in the way similar to the CFL condition. However, it is important to stress that the CFL condition and the Mach number limit are *not* equivalent.

[47] G. Zanetti, Hydrodynamics of lattice-gas automata, Phys. Rev. A 40 (3) (1989) 1539–1548.

[48] R. Brito, M. Ernst, Propagating staggered waves in cellular automata fluids, J. Phys. A 24 (14) (1991) 3331–3349.

[49] D. P. Lockard, L.-S. Luo, S. D. Milder, B. A. Singer, Evaluation of PowerFLOW for aerodynamic applications, J. Stat. Phys. 107 (2002) 423–478.

[50] C. K. Aidun, J. R. Clausen, Lattice-Boltzmann method for complex flows, Annu. Rev. Fluid Mech. 42 (2010) 439–472.

[51] L.-S. Luo, Comment on "Heat transfer and fluid flow in microchannels and nanochannels at high Knudsen number using thermal lattice-Boltzmann method", submitted to Phys. Rev. E (2010).

[52] R. Mei, L.-S. Luo, P. Lallemand, D. d'Humières, Consistent initial conditions for lattice Boltzmann simulations, Comput. Fluids 35 (2006) 855–862.

[53] F. Tosi, S. Ubertini, S. Succi, V. Karlin, Optimization strategies for the entropic lattice Boltzmann method, J. Sci. Comput. 30 (3) (2007) 369–387.

[54] P. Philippi, L. Hegele, L. dos Santos, R. Surmas, From the continuous to the lattice Boltzmann equation: The discretization problem and thermal models, Phys. Rev. E 73 (5) (2006) 056702.

[55] S. Ansumali, I. V. Karlin, Single relaxation time model for entropic lattice Boltzmann methods, Phys. Rev. E 65 (5) (2002) 056312.

[56] F. Dubois, P. Lallemand, M. Tekitek, On a superconvergent lattice Boltzmann boundary scheme, Comput. Math. Appl. 59 (7) (2009) 2141–2149.

[57] The CFL condition requires that $U < \Delta x/\Delta t$, where U is the characteristic velocity of the flow, and Δx and Δt are the grid spacing and the time step size, respectively, both of which are free parameters to be chosen. For the LBE, the incompressibility condition requires that $U/c_s < \mathrm{Ma}_*$, where $\mathrm{Ma}_* \approx 0.3$ is the approximate upper bound of the Mach number, *i.e.*, $U < (\mathrm{Ma}_*/\sqrt{3})\delta_x/\delta_t$. Therefore, the Mach number limit in the LBE can be seen in the way similar to the CFL condition. However, it is important to stress that the CFL condition and the Mach number limit are *not* equivalent.